



# City Research Online

## City St George's, University of London

**Citation:** Rabie, M., Almutairi, F. F., Tsavdaridis, K. & Shaaban, I. G. (2026). Machine Learning-Driven Capacity Design and Embodied Carbon Reduction Optimization in Composite Reduced Web Section (RWS) Connections. *Advances in Engineering Software*, 217, 104145. doi: 10.1016/j.advengsoft.2026.104145

This is the accepted version of the paper.

This version of the publication may differ from the final published version. To cite this item please consult the publisher's version.

**Permanent repository link:** <https://openaccess.city.ac.uk/id/eprint/37036/>

**Link to published version:** <https://doi.org/10.1016/j.advengsoft.2026.104145>

**Copyright and Reuse:** Copyright and Moral Rights remain with the author(s) and/or copyright holders. Copies of full items can be used for personal research or study, educational, or not-for-profit purposes without prior permission or charge, unless otherwise indicated, provided that the authors, title and full bibliographic details are credited, a hyperlink and/or URL is given for the original metadata page and the content is not changed in any way. For full details of reuse please refer to [City Research Online policy](#).

1  
2  
3 **Machine Learning-Driven Capacity Design and Embodied Carbon**  
4 **Reduction Optimization in Composite Reduced Web Section (RWS)**  
5 **Connections**

6 **Mohamed Rabie<sup>1</sup>, Fahad Falah Almutairi<sup>2</sup>, Konstantinos Daniel Tsavdaridis<sup>3,\*</sup>, and**  
7 **Ibrahim G. Shaaban<sup>1</sup>**  
8

9 <sup>1</sup>School of Computing and Engineering, University of West London, St Mary's Road, Ealing W5  
10 5RF, London, UK

11 <sup>2</sup>Department of Civil & Architectural Engineering, College of Engineering, International  
12 University of Science and Technology, Kuwait

13 <sup>3</sup>Department of Engineering, School of Science & Technology, City St George's, University of  
14 London, Northampton Square, EC1V 0HB London, UK

15  
16 \*Corresponding Author: [konstantinos.tsavdaridis@city.ac.uk](mailto:konstantinos.tsavdaridis@city.ac.uk)  
17

18 **ABSTRACT**

19 A gap in current predictive modelling approaches limits the ability to accurately assess the  
20 mechanical, durability performance and sustainability metrics of Reduced Web Section (RWS)  
21 connections. This paper addresses this gap by developing an ensemble machine learning (ML)  
22 framework combined with multi-objective optimisation, enabling the efficient prediction of seven  
23 key mechanical and ductility properties alongside total embodied carbon (EC) reduction. Three  
24 ensemble ML models—Extra Trees Regressor (ETR), Gradient Tree Boosting (GTBR), and  
25 Extreme Gradient Boosting (XGBoost)—were evaluated, with XGBoost demonstrating superior  
26 generalization across most outputs. Additionally, Shapley Additive Explanations (SHAP) analysis  
27 was conducted to identify the most influential design parameters, improving model interpretability.  
28 The multi-objective optimisation performed using NSGA-II, generated Pareto-optimal solutions,  
29 highlighting trade-offs between structural performance and sustainability considerations. The  
30 findings reveal that cross-sectional properties, material stiffness, and connection type significantly  
31 impact RWS performance, and optimising these parameters can lead to improved ductility,  
32 moment capacity, and reduced environmental impact. To enhance practical applicability, a user-  
33 friendly interface was developed and deployed via Hugging Face, allowing users to test the results,  
34 make predictions and retrieve optimal design parameters based on the nearest Pareto-optimal  
35 solutions. The results of this paper demonstrate that ensemble ML methods, coupled with  
36 optimisation and explainability tools, provide a robust framework for advancing RWS connection  
37 design, ensuring both seismic resilience and sustainability in structural engineering.  
38

39 *Keywords:* Reduced Web Section (RWS) Connections, Ensemble Machine Learning, Multi-  
40 Objective Optimisation, Sustainable Structural Design, Embodied Carbon.  
41

## 42 List of Notations

$d_o$	Web opening diameter.
$S_e$	End-distance from column/connection face to centreline of web opening.
$h_c$	Column section height/depth
$b_{cf}$	Steel column flange width
$t_{cf}$	Steel column flange thickness
$t_{cw}$	Steel column web thickness
$L_c$	Column length (distance between supports or loading points)
$A_a$	Beam section cross-sectional area.
$h_b$	Steel beam depth
$b_{bf}$	Steel beam flange width
$t_{bf}$	Steel beam flange thickness
$t_{bw}$	Steel beam web thickness
$L_b$	Beam span
$r_y$	Radius of gyration of steel beam
$f_{ync}$	Column nominal yield stress
$E_{column}$	Column modulus of elasticity
$f_{ynb}$	Beam nominal yield stress
$E_{beam}$	Beam modulus of elasticity
$f_c$	Concrete measured characteristic compressive strength.

43

## 44 1. Introduction

45 There has been successful research in developing fuse strategies that cluster deformation demand  
46 away from the column face, well within the beam [1–3]. However, this approach involves the  
47 extensive intervention of the column and provision of stocky supplemental plates on flanges and  
48 the web, making retrofitting of structures complex, particularly if they were not designed with  
49 full consideration of capacity design principles. On other hand, the escalating climate crisis  
50 necessitates a re-evaluation of civil engineering practices, as steel production generates 1-3  
51 metric tons of carbon emissions per metric ton [4] and UK structural concrete emits  
52 approximately 250 kgeCO<sub>2</sub> equivalent per cubic meter [5]. Reduced Web Section (RWS)  
53 connection emerges as a promising solution in this context, acting as a ductile fuse and  
54 economically addressing the limitations of traditional connections. These rely on perforations  
55 made on the beam’s web rather than flange trimming or the use of supplemental plates to increase  
56 moment capacity at the column’s face. In particular, it is easier to cut through webs than remove

57 floors to intervene on dysfunctional beam flanges.

58 Absorbing seismic demand energy within the RWS connections localise failures, through  
59 fostering a Vierendeel mechanism that enhances seismic performance and mitigates asymmetric  
60 yield effects [6–11]. Such mechanism ensures that critical gravity load-bearing columns remain  
61 protected from extensive plastic deformation and potential structural failure during seismic  
62 events. Such connection simplifies manufacturing and retrofitting and helps prevent out-of-plane  
63 instability. These practical implications underscore the importance of our research in the field of  
64 seismic engineering.

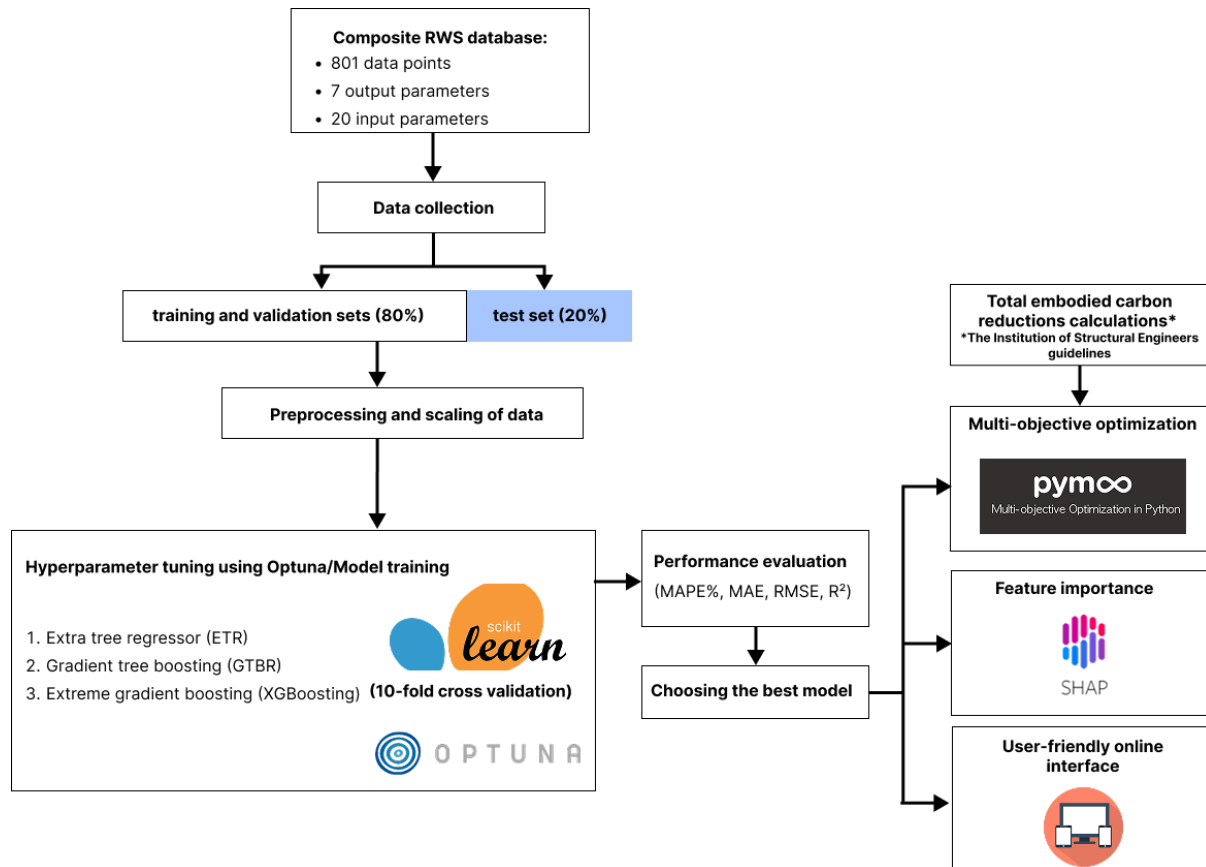
65 The absence of a systematic design methodology to control the seismic performance of  
66 RWS connections through key geometric parameters has driven significant efforts over the past  
67 decade to develop robust guidance, numerical models, and acceptance criteria [6,7,10,12–17].  
68 These studies have indicated that the response of structural moment frames (SMFs) can be  
69 assessed by evaluating the extent of damage it undergoes during a non-linear analysis, which  
70 mimics realistic seismic conditions. By altering the geometry of the RWS (i.e., web opening size  
71 and location) connections can influence its seismic response, providing opportunities to enhance  
72 the overall performance and resilience of the SMFs [8,18–21]. Still, no comprehensive analytical,  
73 mechanical or empirical model are currently available that account for all the design parameters  
74 affecting the non-linear response of RWS connections. This complexity arises from the multiple  
75 deformable components within the steel-concrete composite joint (e.g., column, connection, and  
76 beam) accurate prediction using simple regression analysis which is not sufficient to capture such  
77 complexity. The ability of machine learning to address this complex issue holds significant  
78 promise, offering potential computational techniques that could synthesise complex multi-  
79 parameter interactions and develop more predictive, comprehensive models in structural  
80 engineering field [22–24].

81 The application of ensemble machine learning (ML) models in predicting the properties of  
82 RWS connections presents a significant advancement in structural engineering applications.  
83 Traditional empirical or numerical approaches often struggle to generalize across varying  
84 geometric and material properties, particularly due to the nonlinear interactions between multiple  
85 design parameters such as web opening size, location, and section stiffness [25–27]. Ensemble  
86 ML techniques, including bagging and boosting methods, have proven to be highly effective in

87 structural performance prediction due to their ability to capture complex dependencies, reduce  
88 variance, and improve generalization accuracy [28–31]. Specifically, ensemble models such as  
89 Gradient Boosting, and Extreme Gradient Boosting (XGBoost) leverage multiple weak learners  
90 to construct a more robust predictive framework, mitigating overfitting and enhancing model  
91 stability across diverse datasets. Studies have shown that ensemble-based approaches outperform  
92 single-model regression techniques in predicting structural behavior, including seismic  
93 performance, material strength, and damage assessment [32,33]. Given the highly nonlinear  
94 nature of RWS connections, utilizing ensemble ML provides a computationally efficient  
95 alternative to iterative numerical simulations, enabling rapid design exploration and performance  
96 optimization.

97 Moreover, recent advancements in ML interpretability techniques, such as Shapley  
98 Additive Explanations (SHAP) and permutation feature importance, further reinforce the  
99 applicability of ensemble methods in structural engineering. These techniques allow for  
100 transparent decision-making by identifying the most influential parameters governing RWS  
101 connection behavior, thus bridging the gap between data-driven modelling and engineering  
102 intuition [34,35]. Unlike black-box deep learning models, ensemble-based approaches maintain  
103 a balance between predictive power and interpretability, making them particularly suitable for  
104 engineering applications where explainability is crucial [36]. Furthermore, one of the key  
105 advantages of RWS connections is their sustainability, as they require less steel compared to  
106 conventional connections, reducing material consumption and overall embodied carbon. This  
107 makes RWS connections particularly valuable in the context of sustainable structural design,  
108 where optimizing material efficiency without compromising structural integrity and seismic  
109 performance is a priority [37]. Integrating RWS connections into the capacity design framework  
110 and multi-objective optimization process is essential, yet research in this area remains limited.  
111 Optimizing RWS connections not only enhances structural durability and performance but also  
112 contributes to sustainability efforts by reducing material consumption and embodied carbon. This  
113 aligns with global initiatives aimed at minimizing the environmental impact of the construction  
114 industry while improving structural resilience [38]. Given these advantages, this study aims to  
115 develop an ensemble ML-driven framework to predict the mechanical properties and  
116 sustainability performance of RWS connections, leveraging multi-objective optimisation to

117 balance mechanical, ductility performance and embodied carbon reduction. By integrating  
 118 machine learning, optimisation, and explainability tools, this research aims to provide a  
 119 systematic data-driven approach for the design and performance assessment of RWS  
 120 connections, addressing the current knowledge gaps in empirical and numerical modelling  
 121 approaches as illustrated in Figure 1.



122  
 123 **Figure 1.** Flowchart of the ML process with the user-friendly interface.  
 124

## 125 2. Research Significance

126 Despite extensive research on RWS connections, a significant gap remains in the development of  
 127 systematic, data-driven methodologies for predicting their mechanical performance and  
 128 sustainability metrics. Existing studies primarily rely on empirical models, numerical simulations,  
 129 or experimental testing, which, while valuable, are often computationally expensive, time-  
 130 consuming, and limited in generalizability across different design configurations. Furthermore,  
 131 current analytical and numerical approaches struggle to account for the complex nonlinear

132 interactions between key geometric parameters, material properties, and connection behavior  
133 under seismic loading. While some studies have attempted to optimize RWS designs, there is a  
134 lack of comprehensive multi-objective optimisation frameworks that simultaneously balance  
135 seismic performance and environmental impact. Additionally, machine learning applications in  
136 RWS design remain underexplored, with most prior work in structural engineering focusing on  
137 material property prediction or damage assessment rather than holistic connection performance  
138 modelling. The absence of interpretable, ensemble-based machine learning models that can  
139 effectively predict multiple mechanical properties while providing insights into feature importance  
140 further underscores the need for this research. By addressing these limitations, this study fills a  
141 critical gap in the literature by developing an ensemble ML-driven predictive framework combined  
142 with multi-objective optimisation, enabling more accurate, efficient, and sustainable design  
143 strategies for RWS connections.

144

### 145 3. Methodology

#### 146 3.1. Data description

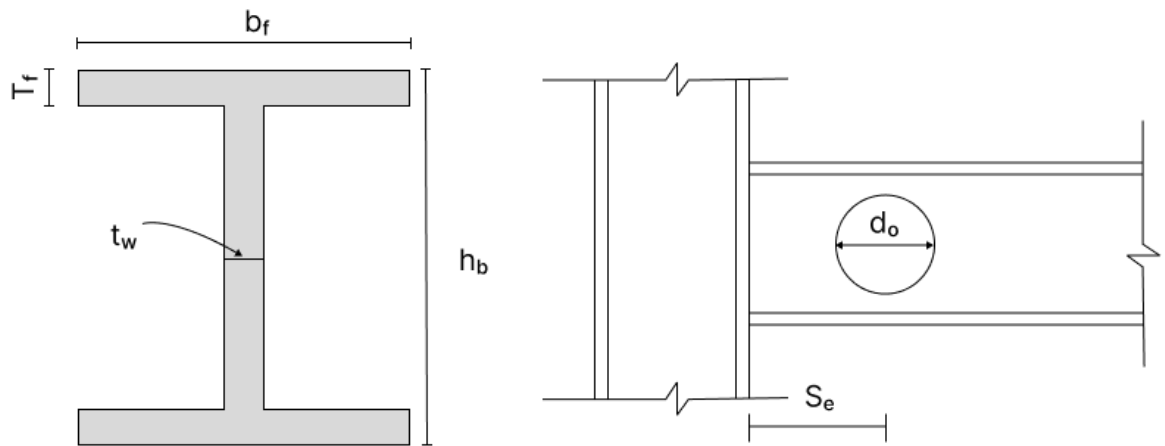
147 A comprehensive database of RWS connections has been assembled, encompassing data  
148 from 16 test and finite element (FE) programmes as illustrated in Table 1, Figure 2 and Figure 3.  
149 For each test specimen, 150 parameters were systematically extracted and tabulated to provide a  
150 complete characterization. These parameters include the primary attributes of the test programme,  
151 geometric properties, material characteristics, and response variables. In this study, the selected  
152 parameters, refined from the initial set based on the most relevant predictors, are tabulated in Table  
153 2. The database was standardised using SI units to ensure consistency and is available online as  
154 mentioned in the data availability statement.

155

**Table 1.** Summary breakdown of the collected RWS database.

Ref.	Total tested specimens/FE models	Study	Connection	Column Section	Beam Section
Guo et al. (2011) [39]	14	FE	Welded	H500×350×14×18	H600×250×10×14
Li et al., (2011) [40]	4	Exp	Welded	H450×300×12×16	H400×200×8×12
Tsavdaridis et al., (2014) [13]	10	FE	Welded	HEB 300	HEA 240
Tsavdaridis and Papadopoulos, (2016) [41]	2	FE	BEEP-3-R	HEB 160	IPE 300
Shin et al., (2017) [42]	2	Exp	WUF-B	W14X145	W12X50 W16X40
Erfani and Akrami, (2017) [7]	1	FE	Welded	HB500x200x10x16	HB414x405x18x28
Shaheen et al., (2018) [19]	13	FE	PN	HB428x407x20x35	HB700x300x13x24
Zhang et al., (2019) [43]	5	FE & Exp	Welded	HW250x250x9x14	HN300x150x6.5x9
Boushehri et al., (2019) [18]	148	FE	Welded	HEB 300, 450, 500, 650	IPE 330, 450, 500, 600
Nazaralizadeh et al., (2020) [11]	1	FE	BEEP-4-R	HEB 200	IPE 270
Tsavdaridis et al., (2021) [10]	1	Exp	BEEP-3-R	UC 203 x 203 x 71	UB 305 x 127 x 48
Xu et al., (2022) [44]	6	Exp	Welded	HW250x250x9x14	HN300x150x6.5x9
Almutairi et al., (2023) [20]	48	FE	BEEP-4-R	HEB 320	IPE 300
Almutairi et al. (2024) [8]	3	Exp	BEEP-4-R	UC 305 x 305 x 198	UB 305 x 165 x 54
Almutairi and Tsavdaridis, (2024) [6]	543	FE	BEEP-4-R	310 UC 158	310 UB 32.0

Note: # = number. FE = Finite element analysis. Exp. experimental test. BEEP-3-R and 4-R = bolted extended end-plate with 3 rows and 4 rows, respectively. WUF-B = welded unreinforced flange-bolted web. PN = pre-Northridge.



160

161

**Figure 2.** RWS connection beam and opening parameters.

162

163  
164

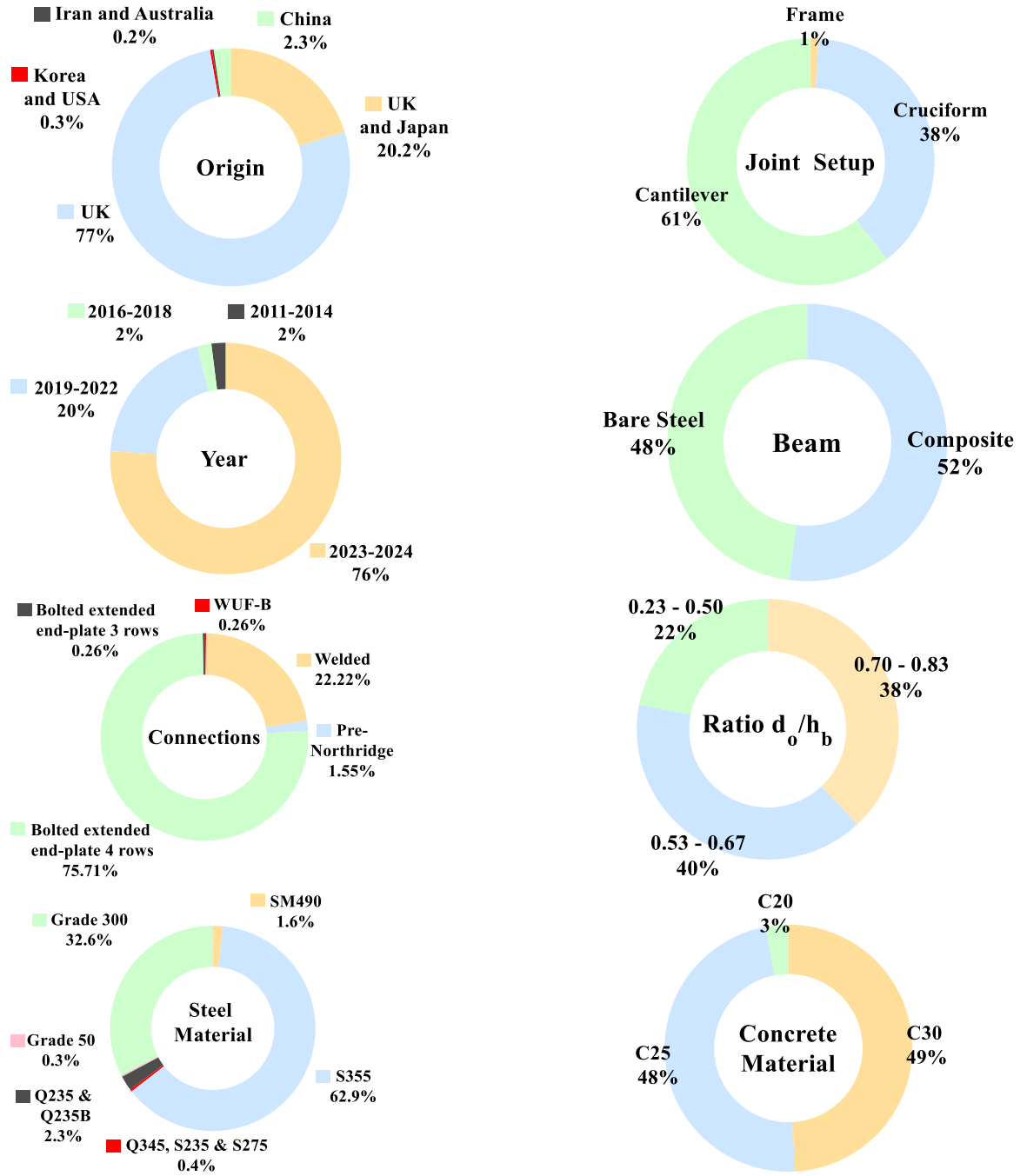


Figure 3. Disaggregated description of assembled RWS databases.

165

166 This database encompasses both bare steel and composite RWS connections, as well as  
167 benchmarked solid webbed-beam connections. The database accounts for different types of test  
168 setups, namely, cantilever, cruciform and frame arrangements, with load and/or displacement is  
169 applied at the beam, or the column ends. Data for both welded and bolted extended end-plate  
170 connections are included, featuring configurations with three or four rows of bolts. Additionally,  
171 the database captures variations in steel and concrete cross-sectional geometries, nominal and  
172 measured material properties, from specifications of different countries.

173 The database was compiled and analysed as detailed in Almutairi and Tsavdaridis (2020)  
174 [6]. The selection criteria were defined to ensure a robust and relevant dataset for both non-seismic  
175 and seismic design applications, focusing on: (1) connections with a single circular web opening  
176 to standardize geometric analysis; (2) inclusion of detailed experimental or FE data to ensure  
177 reliability; and (3) coverage of monotonic and cyclic loading conditions, with monotonic loading  
178 specifically added to evaluate non-seismic performance and cyclic loading to assess seismic  
179 resilience through metrics such as ductility, moment capacity, and energy dissipation. through  
180 metrics such as ductility, moment capacity, and energy dissipation.

181 The descriptive statistics of the dataset, which consists of 801 RWS connection samples is  
182 shown in Table 2, covering a range of geometric, material, and mechanical properties. The dataset  
183 includes five connection types, with the Bolted Extended End-Plate (4 rows) configuration being  
184 the most common, followed by the Welded Connection, Pre-Northridge, Bolted Extended End-  
185 Plate (3 rows), and WUF-B. The geometric parameters show considerable variation, with web  
186 opening diameter ( $d_o$ ) ranging from 0 to 525 mm, End-distance of a web opening ( $S_e$ ) varying  
187 from 0 to 1675 mm (mean = 353.74 mm), and column height ( $h_c$ ) ranging between 160 mm and  
188 650 mm (mean = 362.12 mm). The flange thickness ( $t_{bf}$ ) ranges from 8 mm to 28 mm, while the  
189 web thickness ( $t_{bw}$ ) spans from 6 mm to 18 mm, influencing the capacity metrics of the RWS  
190 connections. The material properties also exhibit variability, with column yield strength ( $f_{ynC}$ ) and  
191 beam yield strength ( $f_{ynB}$ ) averaging 338.25 MPa and 336.69 MPa, respectively, while concrete  
192 compressive strength ( $f_c$ ) varies widely from 0 to 38.08 MPa. While all geometric descriptors of  
193 the RWS perforation are treated as continuous inputs, the ensemble framework exclusively utilizes  
194 one-hot encoding for the categorical connection types to effectively distinguish between the  
195 discrete structural topologies.

**Table 2.** Descriptive statistics of the dataset.

Parameters	Mean	Standard deviation	Minimum	Maximum	Count
Connection Bolted extended end-plate (3 rows)	-	-	-	-	3
Connection Bolted extended end-plate (4 rows)	-	-	-	-	595
Connection Pre-Northridge	-	-	-	-	13
Connection WUF-B	-	-	-	-	2
Connection welded	-	-	-	-	188
$d_o$	214.58	80.08	0.00	525.00	801.00
$S_e$	353.74	223.62	0.00	1675.00	801.00
$h_c$	362.12	82.32	160.00	650.00	801.00
$b_{cf}$	310.21	19.54	160.00	407.00	801.00
$t_{cf}$	26.95	4.67	13.00	35.00	801.00
$t_{cw}$	16.30	2.78	8.00	20.00	801.00
$L_c$	3284.44	4122.22	1090.00	20000.00	801.00
$A_a$	5275.77	2789.89	2649.60	25068.80	801.00
$h_b$	346.06	96.52	230.00	700.00	801.00
$b_{bf}$	169.64	29.72	125.30	405.00	801.00
$t_{bf}$	12.09	3.53	8.00	28.00	801.00
$t_{bw}$	7.70	1.72	6.00	18.00	801.00
$L_b$	4261.46	3785.87	1070.00	20000.00	801.00
Ry	38.28	6.76	27.40	102.00	801.00
$f_{ynC}$	338.25	26.81	235.00	413.70	801.00
E(column)	201617.05	2950.24	193000.00	210000.00	801.00
$f_{ynB}$	336.69	29.59	235.00	372.33	801.00
E(beam)	205089.93	4426.57	176500.00	211331.75	801.00
$f_c$	17.56	17.41	0.00	38.08	801.00
Yield Moment	327.17	297.20	71.14	2318.55	801.00
Maximum Moment	399.68	343.37	101.76	2488.69	801.00
Ultimate Moment	386.02	347.10	80.10	2488.70	801.00
Dissipated Energy	21.36	10.93	2.49	83.91	801.00
Equivalent Viscous Damping	0.26	0.05	0.06	0.59	801.00
Ductility Under Sagging	3.41	0.84	1.67	7.76	801.00
Ductility Under Hogging	3.71	0.94	1.67	7.76	801.00

197

198

199

200

In total, the database comprises 801 test specimens and FE models of RWS connections, including 20 benchmarked solid webbed-beam counterparts. Despite its extensive scope, a small number of experimental and FE programmes were excluded due to insufficient test or modelling

201 details. This database represents a valuable resource for advancing the understanding and  
202 development of RWS connections for seismic-resistance structural design.

203         Although this study does not directly perform seismic simulations or nonlinear FE analysis,  
204 it is grounded in the well-established role of RWS connections in seismic-resistant design. RWS  
205 detailing is intended to promote ductile behavior through the formation of a Vierendeel mechanism  
206 during cyclic loading. The dataset used in this study was compiled from prior test and FE  
207 programmes that specifically evaluated the seismic performance of RWS connections. Therefore,  
208 while this paper focuses on developing predictive models rather than performing new seismic  
209 analyses, the machine learning framework is inherently informed by seismic design considerations.  
210 This includes the prediction of cyclic performance indicators such as moment capacity, rotational  
211 ductility, and energy dissipation. By abstracting this behavior through ensemble ML models, the  
212 study addresses a key gap in current seismic connection design: the lack of accurate, interpretable,  
213 and scalable tools for predicting the seismic and sustainability performance of RWS connections.

214

### 215         3.2. Pre-processing of data using correlation matrix

216         The correlation matrix provides valuable insights into the relationships between input  
217 features and output variables in the prediction of RWS connection properties illustrated in Figure  
218 4. A strong positive correlation is observed among Yield Moment, Maximum Moment, and  
219 Ultimate Moment, with correlation coefficients exceeding 0.99, indicating that increasing the  
220 flexural strength of the connection generally enhances all three moment capacities. Similarly,  
221 Ductility Under Sagging and Ductility Under Hogging exhibit a moderate correlation, suggesting  
222 that improving the ductile response in one loading direction can contribute to enhanced  
223 deformation capacity in the opposite direction.



240 parameters for RWS connection design. These included key geometric variables and material  
241 properties. While certain parameters, such as column length ( $L_c$ ) and beam span ( $L_b$ ), exhibited  
242 multicollinearity, both were retained due to their fundamental importance in predicting the  
243 performance of RWS connections.

244 These correlation patterns highlight the complex interactions governing RWS  
245 connections, emphasizing the importance of using ML to understand this complex interaction  
246 and providing accurate predictive modelling. In addition, utilizing multi-objective optimisation  
247 in balancing capacity design and sustainability.

248

### 249 3.3. Proposed ML models

250 This section presents an overview of the ML models employed in this study. Three  
251 ensemble ML models were evaluated to develop a robust and accurate predictive framework for  
252 the mechanical and ductility properties of composite RWS connections. The study considered  
253 seven output variables, namely Yield Moment, Maximum Moment, Ultimate Moment,  
254 Equivalent Viscous Damping, Energy Dissipated, Ductility Under Hogging, and Ductility Under  
255 Sagging.

256 The selected models were chosen based on their demonstrated effectiveness in regression  
257 tasks in civil engineering applications and their capability to capture complex, non-linear  
258 relationships [45–47], which is an essential characteristic when predicting the intricate  
259 mechanical and ductility behaviors of composite RWS connections as detailed below. It is worth  
260 mentioning that ensemble tree-based methods have also consistently shown superior predictive  
261 accuracy and stability compared with single algorithms and artificial neural networks in structural  
262 engineering applications [48]. It is worth mentioning that a related methodology was reported in  
263 a published work by the first author titled “Glass fibre concrete: Experimental investigation and  
264 predictive modeling using advanced machine learning with an interactive online  
265 interface.”[28,49]. While that study compared both single and ensemble models, the present work  
266 focuses exclusively on ensemble algorithms to better capture the complex input-output  
267 relationships in RWS connections. In addition, this study incorporates multi-objective  
268 optimisation to balance seven mechanical/ductility properties with embodied carbon reduction  
269 and uses a more comprehensive dataset of 801 experimental and finite element cases, offering

270 greater predictive robustness and broader design scope.

271

### 272 3.3.1. Extra tree regressor

273 The Extra Trees Regressor, or Extremely Randomized Trees, is an ensemble-based  
274 machine learning method that extends the principles of the Random Forest algorithm by  
275 incorporating an additional level of randomness into the tree construction process. Unlike  
276 conventional decision tree-based models that optimize split thresholds based on impurity  
277 reduction criteria, Extra Trees selects split points completely at random, thereby increasing  
278 variance among individual trees while maintaining computational efficiency. The algorithm  
279 constructs an ensemble of fully grown decision trees, each trained on the entire dataset rather  
280 than using bootstrap resampling, as is the case with Random Forests. At each node, a random  
281 subset of features is selected, and for each selected feature, a split threshold is chosen at random.  
282 The split that yields the best reduction in variance is then applied to partition the data. This  
283 aggressive randomization reduces variance in the final ensemble while slightly increasing bias,  
284 leading to a robust and computationally efficient model for regression tasks [50].

285

286 Mathematically, the prediction of Extra Trees Regressor follows the general form of an  
287 ensemble averaging method. Given a dataset  $\mathcal{D} = \{(x_i, y_i)\}_{i=1}^N$ , where  $x_i \in R^d$  represents the  
288 feature vector and  $y_i \in R$  is the target variable, the prediction for a new input  $x^*$  is obtained by  
289 averaging the predictions of T individual decision trees as shown in Eq.1 :

290

$$\hat{y}(x) = \frac{1}{T} \sum_{t=1}^T f_t(x) \quad (1)$$

291

292

293 where  $f_t(x)$  is the prediction from the t-th tree in the ensemble. Each decision tree  
294 operates by recursively splitting the feature space using randomly chosen thresholds. At each  
295 internal node, a subset  $\mathcal{S} \subseteq \{1, \dots, d\}$  of K features is randomly selected, and a split threshold  
296  $s_j$  is chosen uniformly at random from the range of values in feature  $x_j$  as shown in Eq. 2:

$$s_j \sim U(x_{j,min}, x_{j,max}) \quad (2)$$

297

298  $x_{j,min}$  and  $x_{j,max}$  the minimum and maximum values of feature  $x_j$  in the current node.

299 The best feature  $j^*$  is then selected by minimizing the weighted variance reduction as shown in

300 Eq. 3:

$$j^* = \arg \min_{j \in \mathcal{S}} \left[ \frac{N_L}{N} \text{Var}(Y_L) + \frac{N_R}{N} \text{Var}(Y_R) \right] \quad (3)$$

301 where  $Y_L$  and  $Y_R$  are the target values of the left and right child nodes, respectively, and

302  $N_L$  and  $N_R$  denote the number of samples in the left and right partitions.

303

304 The final ensemble prediction leverages the decorrelation among trees to enhance  
 305 generalization performance. This strategy makes Extra Trees particularly effective for handling  
 306 high-dimensional data, as well as datasets with noisy or redundant features. Compared to  
 307 Random Forests, Extra Trees are computationally more efficient due to the elimination of the  
 308 search for optimal split points, making them well-suited for large-scale regression tasks [51].

309

### 310 3.3.2. Gradient tree boosting regression

311 The Gradient Tree Boosting Regressor, also known as Gradient Boosted Regression Trees  
 312 (GBRT), is a powerful ensemble learning method that builds a strong predictive model by  
 313 iteratively combining multiple weak learners, typically decision trees, in a stage-wise manner.  
 314 Unlike Random Forests and Extra Trees, which average predictions from independently trained  
 315 trees, gradient boosting builds trees sequentially, with each new tree trained to correct the residual  
 316 errors of the previous trees. The method is grounded in gradient-based optimisation, where each  
 317 new tree minimizes the residual loss using a differentiable loss function, leading to a refined and  
 318 accurate predictive model.

319 Mathematically, given a dataset  $\mathcal{D} = \{(x_i, y_i)\}_{i=1}^N$ , where  $x_i \in R^d$  represents the feature  
 320 vector and  $y_i \in R$  is the target variable, gradient boosting constructs an additive model of T  
 321 decision trees. The model learns a function  $F(x)$  that approximates the mapping from input  $x$  to  
 322 target  $y$  by iteratively refining its predictions as shown in Eq. 4:

$$F_T(x) = F_{T-1}(x) + \eta f_T(x) \quad (4)$$

323

324

325

326

where  $f_T(x)$  is the prediction from the newly added decision tree at iteration T, and  $\eta$  (the learning rate) controls the contribution of each tree to the final model. The function  $F_T(x)$  is initialized with a constant value, often the mean of the target variable as shown in Eq. 5:

$$F_0(x) = \arg \min_c \sum_{i=1}^N L(y_i, c) \quad (5)$$

327

328

329

330

where  $L(y, \hat{y})$  is the chosen loss function, commonly the squared error for regression as shown in Eq. 6:

$$L(y, \hat{y}) = (y - \hat{y})^2 \quad (6)$$

331

332

333

At each iteration, a new tree is fitted to approximate the negative gradient of the loss function with respect to the current model's predictions as shown in Eq. 7:

$$r_i^{(t)} = - \left[ \frac{\partial L(y_i, F_{t-1}(x_i))}{\partial F_{t-1}(x_i)} \right] \quad (7)$$

334

335

336

337

This residual  $r_i^{(t)}$  serves as the pseudo-target for the next tree, which is then trained to minimize the mean squared error with respect to these gradients. The final prediction is obtained by summing the outputs of all trees in the ensemble as shown in Eq. 8:

$$\hat{y}(x) = \sum_{t=1}^T \eta f_t(x) \quad (8)$$

338

339

340

341

342

343

One of the key advantages of Gradient Tree Boosting is its ability to model complex, non-linear relationships with high accuracy while maintaining strong generalization performance. The method can be regularized through techniques such as learning rate reduction, limiting tree depth, and incorporating shrinkage or subsampling to prevent overfitting. Compared to Random Forests and Extra Trees, gradient boosting often achieves superior predictive accuracy, particularly in

344 structured data settings, though it requires careful hyperparameter tuning to balance bias-variance  
345 trade-offs [52,53].

346

### 347 3.3.3. Extreme gradient boosting (XGBoost)

348 The Extreme Gradient Boosting (XGBoost) Regressor is an optimized implementation of  
349 gradient tree boosting that enhances computational efficiency, scalability, and predictive  
350 accuracy. As a variant of Gradient Boosted Regression Trees (GBRT), XGBoost constructs an  
351 ensemble of decision trees in a stage-wise fashion, where each new tree corrects the residual  
352 errors of the previous trees. However, XGBoost introduces several key improvements over  
353 standard gradient boosting, including second-order gradient optimization, a regularized objective  
354 function, column block structure for parallelization, and sparsity-aware split finding, making it  
355 particularly well-suited for large-scale regression tasks.

356 Formally, given a dataset  $\mathcal{D} = \{(x_i, y_i)\}_{i=1}^N$ , where  $x_i \in R^d$  represents the feature vector  
357 and  $y_i \in R$  is the target variable, XGBoost builds an additive model of T trees to approximate  
358 the function  $F(x)$  that maps inputs to outputs as shown in Eq. 9:

359

$$F_T(x) = F_{T-1}(x) + \eta f_T(x) \quad (9)$$

360

361 Where  $f_T(x)$  is the new decision tree added at iteration T, and  $\eta$  (the learning rate)  
362 controls its contribution. Unlike traditional gradient boosting, which optimizes using first-order  
363 gradients, XGBoost leverages a Taylor expansion of the loss function up to the second order to  
364 improve optimisation as shown in Eq. 10:

$$L(y, \hat{y}) \approx L(y, F_{t-1}(x)) + g_i f_t(x) + \frac{1}{2} h_i f_t^2(x) \quad (10)$$

365

366 Where  $g_i$  and  $h_i$  are the first-order gradient and second-order Hessian of the loss function,  
367 respectively as shown in Eq. 11:

$$g_i = \frac{\partial L(y_i, F_{t-1}(x_i))}{\partial F_{t-1}(x_i)}, \quad h_i = \frac{\partial^2 L(y_i, F_{t-1}(x_i))}{\partial^2 F_{t-1}(x_i)} \quad (11)$$

368

369 By incorporating second-order derivatives, XGBoost achieves more precise updates,

370 leading to faster convergence and improved predictive performance. Additionally, XGBoost  
371 regularizes the model using an objective function that includes both L1 (Lasso) and L2 (Ridge)  
372 penalties as shown in Eq. 12:

$$\Omega(f_t) = \gamma T + \frac{1}{2} \lambda \sum_{j=1}^T w_j^2 \quad (12)$$

373  
374 where  $\gamma$  controls the complexity penalty for each tree, and  $\lambda$  regulates the magnitude of  
375 leaf weights  $w_j$ . This regularization prevents overfitting and enhances generalization.

376 A major advantage of XGBoost is its efficient computation. By employing a column  
377 block structure for parallel tree construction and a sparsity-aware split-finding algorithm,  
378 XGBoost can handle high-dimensional data with missing values more efficiently than traditional  
379 boosting methods. The combination of gradient-based optimization, regularization,  
380 parallelization, and efficient memory usage makes XGBoost a state-of-the-art approach for  
381 regression tasks [54,55].

382

### 383 3.4. Shapley Additive exPlanations (SHAP)

384 SHAP is a widely used method for interpreting ML model predictions by quantifying the  
385 contribution of each feature to the output. Based on cooperative game theory, SHAP assigns a  
386 Shapley value to each feature, ensuring a fair distribution of contributions by considering all  
387 possible feature combinations. This method provides a consistent and theoretically grounded  
388 approach to feature attribution, making it particularly valuable for understanding complex  
389 models. By illustrating both global and local feature importance, SHAP enhances model  
390 transparency and supports informed decision-making. In this study, SHAP analysis will be  
391 conducted on the best-performing model to assess the relative influence of each feature on its  
392 predictions [56].

393

### 394 3.5. Multi-objective Optimization

395 Multi-objective optimization (MOO) is a critical approach in engineering and materials  
396 science, particularly for balancing competing objectives in structural design. In this study, Non-  
397 dominated Sorting Genetic Algorithm II (NSGA-II) was employed to simultaneously optimize

398 the mechanical and ductility properties of composite RWS connections while incorporating an  
399 additional sustainability objective: minimizing total embodied carbon. The NSGA-II algorithm,  
400 a well-established evolutionary optimisation method, was chosen due to its efficiency in handling  
401 complex, multi-dimensional trade-offs and its ability to maintain a diverse set of Pareto-optimal  
402 solutions [57].

403 The optimization problem was formulated with eight objective functions, including the  
404 seven mechanical and ductility properties—Yield Moment, Maximum Moment, Ultimate  
405 Moment, Equivalent Viscous Damping, Energy Dissipated, Ductility Under Hogging, and  
406 Ductility Under Sagging—alongside total embodied carbon reduction due to the opening in the  
407 web section. These objectives often exhibit conflicting behavior; for instance, enhancing strength  
408 and ductility may lead to increased material usage, thereby elevating embodied carbon emissions.  
409 Thus, an optimisation framework that simultaneously accounts for mechanical performance and  
410 sustainability is essential.

411 The embodied carbon (EC) calculations are based on the Institution of Structural  
412 Engineers (IStructE) guidelines [58]. The scope of the embodied carbon calculations was taking  
413 into account the life-cycle assessment for the modules A1–A5 as illustrated in Figure 5, which  
414 focuses on the embodied carbon calculation up to practical completion stage referred to as cradle-  
415 practical completion. The embodied carbon factors (ECFs) for the structural steel sections were  
416 sourced from the British Steel Environmental Product Declaration (EPD) [59]. Sustainability  
417 was quantified by calculating the total reduction in embodied carbon ( $EC_{reduction}$ ) resulting  
418 from the web perforation. The weight removed was multiplied by the sum of the embodied carbon  
419 factors for modules A1–A3, A4, and A5w (2.45, 0.032, and 0.025, respectively) as shown in Eq.  
420 13.

421

$$EC_{reduction} = W_{(removed)} \times (ECF_{(A1-A3)} + ECF_{A4} + ECF_{A5w}) \quad (13)$$

422 Where  $W_{(removed)}$  represents the weight of the steel removed from the web section. The  
423  $EC_{reduction}$  value was integrated into the NSGA-II algorithm as a primary objective to be  
424 maximized. It is acknowledged that absolute carbon values may vary depending on assumptions

425 such as material sourcing, manufacturing techniques, and installation practices; however, these  
 426 variations do not alter the relative trends or the optimal trade-offs determined in this study.

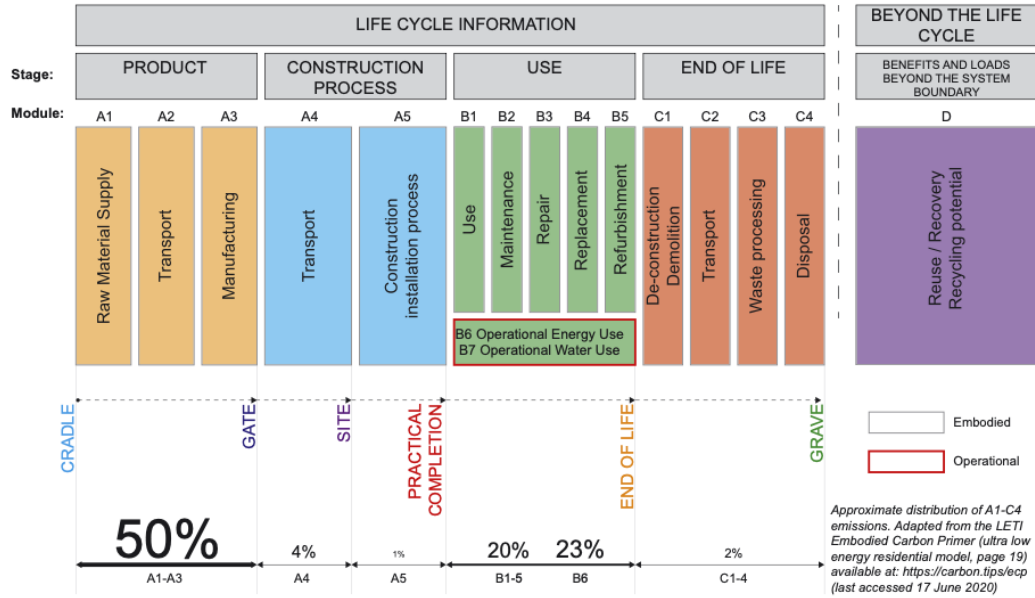


Figure 5. Life cycle assessment stages and modules [60].

427 To address constraints effectively, a custom repair operator was integrated into the  
 428 NSGA-II algorithm to ensure feasible solutions by correcting infeasible candidates based on  
 429 predefined structural constraints. Two primary constraints were applied: (1) all predictor  
 430 variables were restricted to remain within the upper and lower bounds of the compiled dataset,  
 431 ensuring that generated solutions represent realistic and physically attainable designs; and (2) the  
 432 predicted yield moment was required to be less than or equal to the predicted maximum moment,  
 433 maintaining mechanical consistency with established structural behavior. The optimisation  
 434 process was carried out with a population size of 20 over 500 generations, leveraging constraint  
 435 handling and duplicate elimination to enhance solution diversity and convergence toward an  
 436 optimal trade-off front.

437 The NSGA-II algorithm operates by maintaining a Pareto front, where solutions are  
 438 ranked based on dominance relationships, ensuring a diverse distribution of trade-off solutions  
 439 between mechanical performance and sustainability [61,62]. By applying this evolutionary

440 approach, the study identifies a set of optimal design alternatives that balance structural  
441 efficiency with environmental impact, aiding in the development of more sustainable and high-  
442 performance composite RWS connections.

443

### 444 3.6. User-friendly interface

445 A user-friendly interface was developed using Gradio V4.36.1 and deployed online via  
446 Hugging Face to facilitate predictive modeling in structural engineering. Following a  
447 comprehensive evaluation of multiple ensemble machine learning models, the best-performing  
448 model was selected based on its predictive accuracy and robustness. This optimized model  
449 enables precise estimation of seven mechanical properties—Yield Moment, Maximum Moment,  
450 Ultimate Moment, Equivalent Viscous Damping, Energy Dissipated, Ductility Under Hogging,  
451 and Ductility Under Sagging—along with total embodied carbon reduction. The Gradio interface  
452 allows researchers and engineers to seamlessly integrate this tool into their optimisation  
453 workflows, supporting data-driven decision-making. The trained model files and source code are  
454 available at the following link:

455 ([https://huggingface.co/spaces/MohamedRabie26/RWS\\_connections/tree/main](https://huggingface.co/spaces/MohamedRabie26/RWS_connections/tree/main) ).

456

## 457 4. Criteria for performance evaluation & hyperparameter selection

### 458 4.1. Performance evaluation criteria

459 Optimal outcomes in data-driven models require continuous performance assessment  
460 during training. In this study, the Optuna library was used for efficient hyperparameter  
461 optimisation. Each machine learning model was trained and tuned using 10-fold cross-validation,  
462 in which the training dataset was randomly partitioned into ten equal subsets. In each fold, nine  
463 subsets were used for training and one for validation, cycling through all combinations. The final  
464 model configuration was chosen based on the average validation performance across the folds,  
465 ensuring robust hyperparameter selection and improved generalization to unseen data. This  
466 approach was preferred over holding out an additional independent dataset, as it allows for efficient  
467 use of the available data while still providing multiple rigorous evaluations on unseen subsets,  
468 thereby reducing the risk of overfitting. The performance of different ML models was evaluated  
469 using four metrics: Mean Absolute Percentage Error (MAPE), Mean Absolute Error (MAE), Root

470 Mean Squared Error (RMSE), and the Coefficient of Determination ( $R^2$ ), as defined in Eqs. 14-  
471 17:

$$MAPE = \frac{100}{n} \sum_{i=1}^n \left| \frac{y_i - \hat{y}_i}{y_i} \right| \quad (14)$$

$$MAE = \frac{1}{n} \sum_{i=1}^n |y_i - \hat{y}_i| \quad (15)$$

$$RMSE = \sqrt{\frac{1}{n} \sum_{i=1}^n (y_i - \hat{y}_i)^2} \quad (16)$$

$$R^2 = 1 - \frac{\sum_{i=1}^n (y_i - \hat{y}_i)^2}{\sum_{i=1}^n (y_i - \bar{y})^2} \quad (17)$$

472 where  $y_i$  and  $\hat{y}_i$  are the target and predicted values, respectively,  $\bar{y}$  is the mean of values,  
473 and  $n$  is the number of data points.

474 A brief description of the statistical metrics used in evaluating each ML model is as  
475 follows:

- 476 • Mean Absolute Percentage Error (MAPE): MAPE measures the average percentage  
477 deviation between predicted and actual values, providing an intuitive understanding of  
478 prediction accuracy. It is particularly useful for comparing model performance across  
479 different datasets with varying scales.
- 480 • Mean Absolute Error (MAE): MAE quantifies the average magnitude of errors in  
481 predictions, without considering their direction. Its straightforward interpretation makes it  
482 a reliable metric for assessing the overall prediction quality of machine learning models.
- 483 • Root Mean Squared Error (RMSE): RMSE highlights the magnitude of larger errors by  
484 giving more weight to significant deviations due to its squaring process. This makes it an  
485 essential metric for detecting models that fail to capture extreme variations in the  
486 mechanical properties of AAM.
- 487 • Coefficient of Determination ( $R^2$ ):  $R^2$  measures the proportion of variance in the target  
488 variable explained by the model. It is critical for understanding how well a model captures  
489 the underlying patterns in the data, reflecting its overall goodness-of-fit.

490 These metrics collectively provide a comprehensive evaluation framework, ensuring that both  
491 accuracy and robustness of the machine learning models are effectively assessed for predicting  
492 the mechanical and ductility properties of RWS connections.

493 A superior model exhibits lower MAE and RMSE values, coupled with a higher  $R^2$  value.  
494 Where overfitting of a model shows higher error metrics on the test set compared to the training  
495 set and a significant discrepancy between training and test  $R^2$  values.

496

#### 497 4.2. Hyper parameter selection

498 Hyperparameters are critical for the performance and accuracy of a ML model, requiring  
499 careful optimisation. This study uses Optuna, a robust hyperparameter optimization framework, to  
500 fine-tune model parameters. Optuna is more efficient and flexible than traditional grid search,  
501 effectively handling high-dimensional and non-convex parameter spaces. It also prunes  
502 unpromising trials early, saving computational resources. Detailed optimized hyperparameter  
503 values and best-performing settings are summarized in Table 3. Further information on Optuna  
504 can be found in [63].

**Table 3.** Optuna optimized hyperparameters.

Model	Hyperparameter Range	$M_y$	$M_m$	$M_u$	Ed	$\zeta_{eq}$	$\theta_u/\theta_y$ +ve	$\theta_u/\theta_y$ -ve
Extra tree regressor (ETR)	max_depth: [3, 500]	375	311	299	268	141	12	89
-	max_features: ['log2', 'sqrt']	sqrt	log2	sqrt	sqrt	log2	log2	sqrt
-	min_samples_leaf: [1, 50]	1	1	1	1	9	1	1
-	min_samples_split: [2, 100]	2	4	5	10	1	2	6
-	n_estimators: [10, 1000]	228	928	917	78	283	558	111
-	random_state: [5]	5	5	5	5	5	5	5
Gradient tree boosting (GTB)	n_estimators: [50, 2000]	1527	1846	620	86	232	1919	178
-	max_depth: [4, 100]	78	4	4	9	96	45	74
-	learning_rate: [0.01, 0.9]	0.074	0.165	0.318	0.168	0.095	0.010	0.089
-	subsample: [0.2, 0.9]	0.455	0.615	0.370	0.802	0.719	0.888	0.807
-	max_features: [7, 100]	7	7	7	7	9	95	10
-	min_samples_split: [2, 50]	25	14	47	24	46	48	47
-	min_samples_leaf: [1, 50]	19	23	14	28	27	7	6
-	random_state: [5]	5	5	5	5	5	5	5
Extreme gradient boosting (XGBoosting)	n_estimators: [50, 2000],	1464	1775	1062	1557	851	1467	1132
-	'max_depth': [4, 40],	35	5	23	29	30	28	8
-	'learning_rate': [0.01, 0.99],	0.071	0.065	0.500	0.210	0.233	0.101	0.104
-	'subsample': [0.1, 0.9],	0.587	0.802	0.704	0.869	0.776	0.547	0.736
-	'colsample_bylevel': [0.1, 0.9],	0.880	0.421	0.750	0.795	0.848	0.562	0.304
-	'colsample_bynode': [0.1, 1.0],	0.458	0.570	0.511	0.401	0.911	1.000	0.976
-	'colsample_bytree': [0.1, 1.0],	0.818	0.835	0.628	0.983	0.414	0.740	0.858
-	'reg_alpha': [0, 0.9],	2.03E-05	0.016	0.158	0.886	0.198	0.426	0.066
-	'reg_lambda': [0.1, 1],	0.849	0.902	0.892	0.867	0.739	0.566	0.813
-	'gamma': [0.0, 0.1],	1.20E-04	1.39E-05	7.94E-05	0.00118749	6.42E-05	3.37E-05	0.0018
-	'random_state': [5]	5	5	5	5	5	5	5

507 5. Results and discussion

508 5.1. Performance evaluation and explainability analysis of ML models for RWS connections

509 Table 4 presents the performance indices for three machine learning models—Extra Trees  
510 Regressor (ETR), Gradient Tree Boosting Regressor (GTBR), and Extreme Gradient Boosting  
511 (XGBoost)—in predicting seven key outputs for Reduced Web Section (RWS) connections. The  
512 models were evaluated based on Mean Absolute Percentage Error (MAPE %), Mean Absolute  
513 Error (MAE), Root Mean Square Error (RMSE), and the coefficient of determination ( $R^2$ ) for both  
514 the training and test datasets. A comparative analysis of these metrics provides insights into the  
515 predictive accuracy and generalization ability of each model across different mechanical  
516 properties.

517

518 **Table 4.** Performance indices for different ML algorithms in predicting outputs for RWS connections.

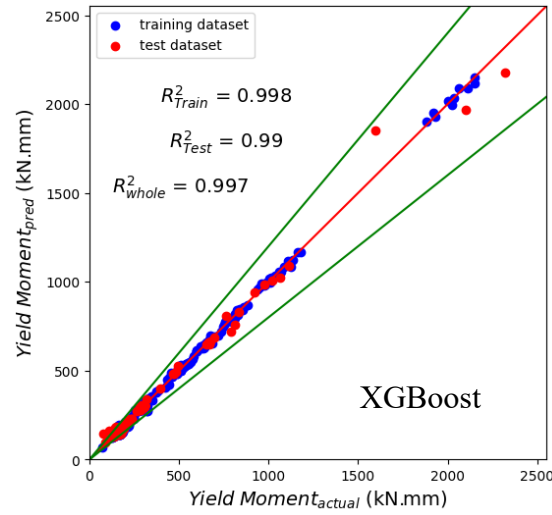
Output	Models	Training dataset				Test dataset			
		MAPE (%)	MAE	RMSE	$R^2$	MAPE (%)	MAE	RMSE	$R^2$
$M_y$	ETR	2.312	0.002	0.00320	0.999	7.034	0.008	0.017	0.984
	GTBR	2.968	0.003	0.00504	0.998	6.169	0.007	0.018	0.982
	XGBoosting	3.906	0.004	0.00542	0.998	5.206	0.006	0.013	0.99
$M_m$	ETR	4.183	0.005	0.00752	0.997	7.835	0.009	0.016	0.989
	GTBR	4.579	0.005	0.00818	0.997	6.746	0.008	0.015	0.989
	XGBoosting	4.572	0.005	0.00725	0.998	6.856	0.007	0.012	0.994
$M_u$	ETR	5.641	0.007	0.01062	0.996	8.916	0.010	0.017	0.987
	GTBR	6.727	0.008	0.01089	0.995	7.936	0.009	0.017	0.987
	XGBoosting	7.347	0.008	0.01146	0.994	8.117	0.009	0.014	0.991
Ed	ETR	7.626	0.015	0.03650	0.909	11.577	0.022	0.059	0.808
	GTBR	8.388	0.016	0.03421	0.917	14.535	0.024	0.075	0.698
	XGBoosting	8.322	0.016	0.03200	0.929	13.411	0.024	0.076	0.685
$\zeta_{eq}$	ETR	2.981	0.013	0.02028	0.956	4.343	0.018	0.028	0.904
	GTBR	3.509	0.014	0.02392	0.937	4.717	0.018	0.03	0.891
	XGBoosting	2.856	0.013	0.01916	0.961	4.216	0.018	0.028	0.908
$\theta_u/\theta_y$ +ve	ETR	2.55	0.014	0.02185	0.975	5.76	0.033	0.063	0.756
	GTBR	1.982	0.011	0.02033	0.978	6.574	0.038	0.068	0.714
	XGBoosting	3.785	0.019	0.02746	0.959	5.099	0.029	0.051	0.842
$\theta_u/\theta_y$ -ve	ETR	4.051	0.025	0.03445	0.954	6.386	0.041	0.065	0.801
	GTBR	3.579	0.022	0.03150	0.962	6.145	0.040	0.064	0.808
	XGBoosting	4.122	0.026	0.03488	0.954	5.711	0.036	0.059	0.839

519 5.1.1. Yield Moment

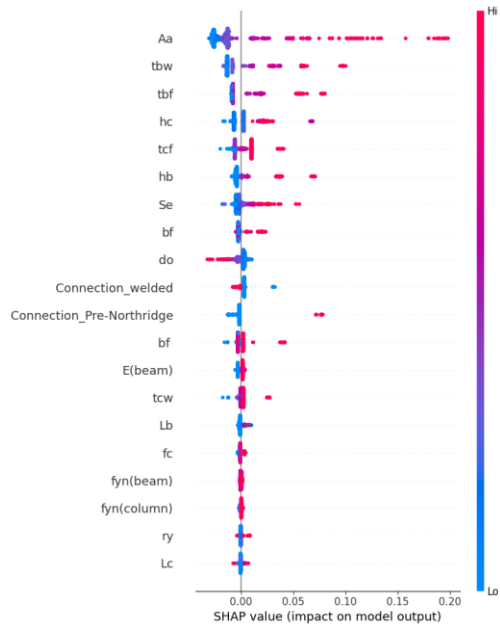
520 The performance evaluation of ML models for predicting Yield Moment ( $M_y$ )  
521 demonstrates that XGBoost is the most effective model, achieving the lowest test MAPE  
522 (5.206%) and the highest  $R^2$  (0.99), indicating superior generalization capability. While ETR  
523 exhibited the lowest training error (MAPE: 2.312%), its higher test error (MAPE: 7.034%)  
524 suggests mild overfitting, whereas GTBR maintained a balanced performance with an  $R^2$  of  
525 0.982 on the test dataset. To further understand the contribution of input features to model  
526 predictions, SHAP analysis was performed on the optimal ML model as shown in Figure 6,  
527 revealing that the cross-sectional area of the beam ( $A_a$ ) is the most influential feature, followed  
528 by web thickness ( $t_{bw}$ ), flange thickness ( $t_{bf}$ ), column depth ( $h_c$ ), and column flange thickness

529 ( $t_{cf}$ ). These results align with fundamental structural mechanics principles [64], where larger  
530 cross-sectional dimensions in particular the distance between the flanges, the higher the distance  
531 the higher the moment capacity. The connection type also plays a notable role, with the “welded”  
532 connection type showing a substantial impact on Yield Moment prediction, highlighting the  
533 significance of stress transfer mechanisms at the connection interface [65]. Features such as  
534 column length ( $L_c$ ), radius of gyration ( $r_y$ ), and column yield strength ( $f_{yn}(column)$ ) were found  
535 to have minimal influence, suggesting that their contribution to  $M_y$  is relatively indirect. The  
536 SHAP summary plot further indicates non-linear feature interactions, particularly for  $A_a$ , which  
537 exhibits a stronger influence at higher values. These insights reinforce the model’s reliability and  
538 interpretability, demonstrating that the machine learning framework successfully captures the  
539 underlying structural behavior of RWS connections.

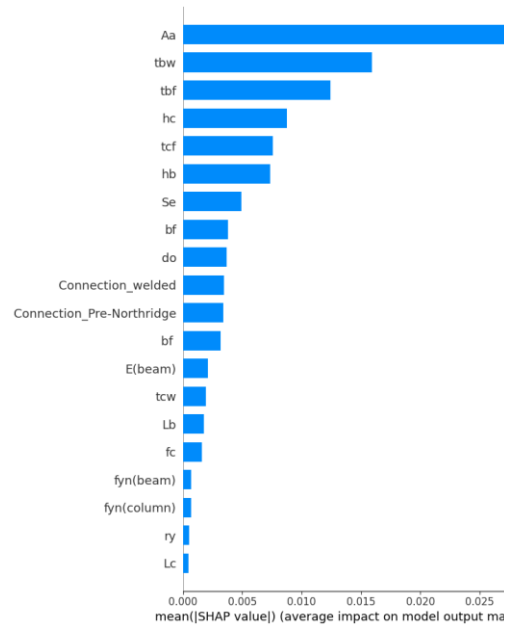
540



(a)



(b)



(c)

542 **Figure 6.** Performance of the optimum ML model in predicting the yield moment of RWS  
 543 connection; (a) Comparison of actual vs. predicted values; (b) SHAP summary plot of the  
 544 predictions; (c) Ranking of feature’s impact on the prediction model.

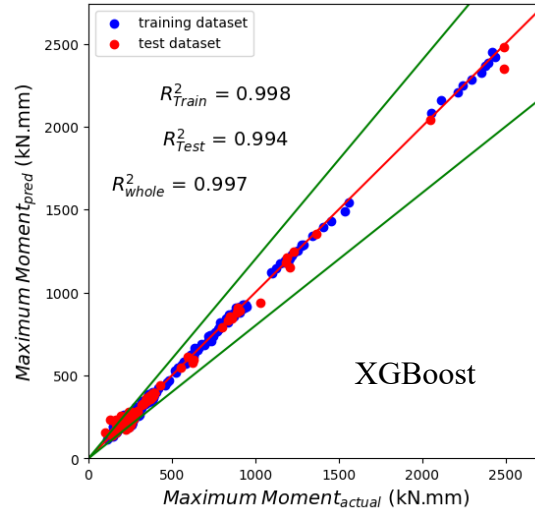
545

546 5.1.2. Maximum Moment

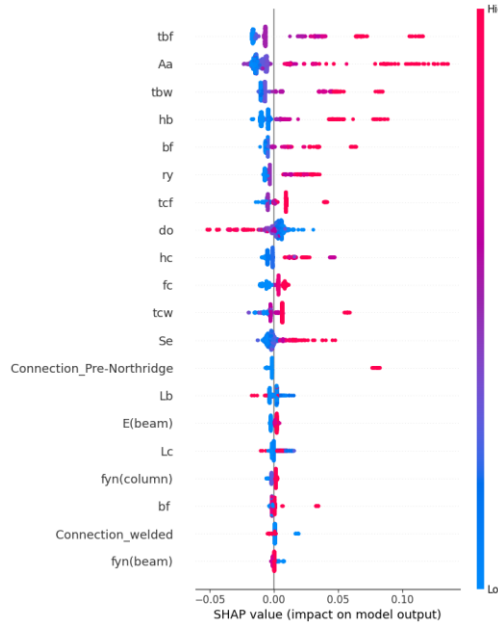
547 The performance evaluation of ML models in predicting Maximum Moment ( $M_m$ )

548 indicates that XGBoost is the most reliable model, achieving the highest  $R^2$  value (0.994) and  
549 the lowest test RMSE (0.012), signifying strong predictive accuracy and generalization. While  
550 ETR exhibited the lowest training error (MAPE: 4.183%), its test error (MAPE: 7.835%)  
551 suggests a degree of overfitting, whereas GTBR performed competitively with a test  $R^2$  of 0.989,  
552 showing balanced performance. To gain further insight into the contribution of individual  
553 features to the model's predictions, SHAP analysis was conducted on the optimal ML model as  
554 shown in Figure 7. The results demonstrate that flange thickness ( $t_{bf}$ ) is the most significant  
555 predictor, followed closely by cross-sectional area ( $A_a$ ), web thickness ( $t_{bw}$ ), and beam height  
556 ( $h_b$ ), all of which play a crucial role in governing the flexural capacity of RWS connections. The  
557 radius of gyration ( $r_y$ ) and column flange thickness ( $t_{cf}$ ) also exhibit substantial influence,  
558 reinforcing the importance of section stiffness and moment resistance. Interestingly, connection  
559 type (e.g., "Pre-Northridge") is moderately impactful, suggesting that different connection  
560 configurations influence moment transfer efficiency. Features such as beam flange width ( $b_f$ ),  
561 column yield strength ( $f_{yn}(\text{column})$ ), and column length ( $L_c$ ) have minimal impact, indicating  
562 that local cross-sectional properties have a stronger influence than global structural dimensions.  
563 The SHAP summary plot further highlights that higher values of  $t_{bf}$  and  $A_a$  are positively  
564 correlated with increased  $M_m$ , aligning with fundamental structural mechanics principles where  
565 larger cross-sectional dimensions enhance moment capacity [66]. These findings confirm that the  
566 XGBoost model effectively captures the non-linear dependencies governing Maximum Moment,  
567 and the SHAP analysis reinforces the physical consistency of the model's predictions.

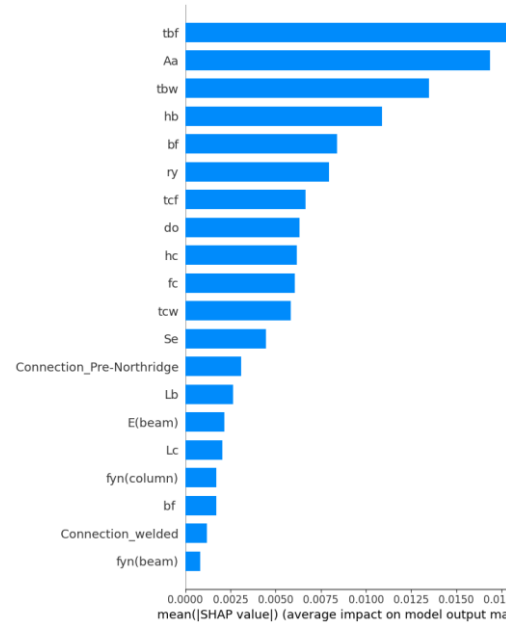
568



(a)



(b)



(c)

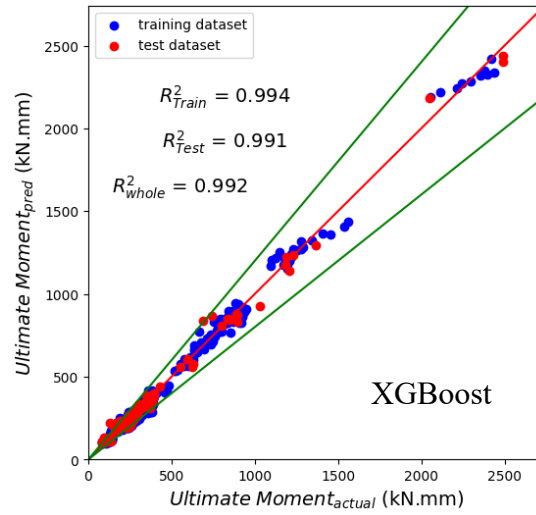
569 **Figure 7.** Performance of the optimum ML model in predicting the maximum moment of RWS  
 570 connection; (a) Comparison of actual vs. predicted values; (b) SHAP summary plot of the  
 571 predictions; (c) Ranking of feature’s impact on the prediction model.

572

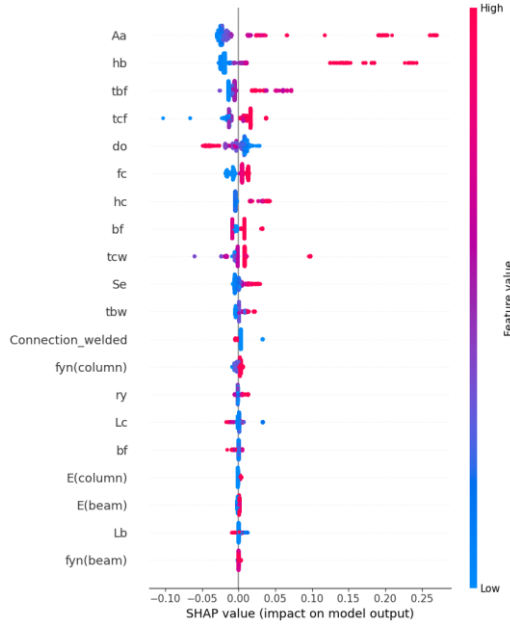
573 5.1.3. Ultimate Moment

574 The evaluation of ML models for predicting Ultimate Moment ( $M_u$ ) reveals that XGBoost  
 575 provides the most reliable generalization, achieving an  $R^2$  of 0.991 on the test dataset, coupled

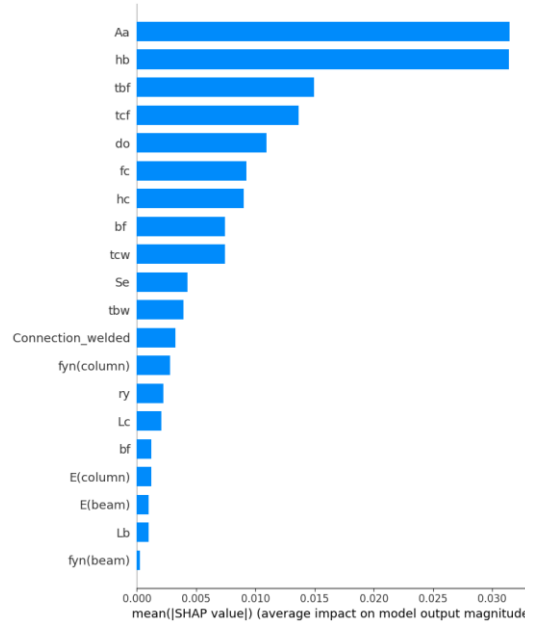
576 with the lowest test RMSE (0.014). While ETR performed well on the training dataset with the  
577 lowest MAPE (5.641%), its test performance (MAPE: 8.916%) suggests a tendency toward  
578 overfitting, whereas GTBR maintained a balanced performance (test MAPE: 7.936%). To further  
579 interpret the model’s decision-making process, SHAP analysis was conducted to quantify the  
580 influence of each feature on Ultimate Moment predictions using the optimum ML model as  
581 shown in Figure 8. The results indicate that cross-sectional area ( $A_a$ ) and beam height ( $h_b$ ) are  
582 the most dominant predictors, highlighting their fundamental role in resisting flexural forces.  
583 Flange thickness ( $t_{bf}$ ), column flange thickness ( $t_{cf}$ ), and column depth ( $h_c$ ) also exhibit a strong  
584 influence, emphasizing the importance of both beam and column stiffness in moment capacity.  
585 Interestingly, the diameter of the openings ( $d_o$ ) appears to have a significant impact, likely due  
586 to its effect on stress redistribution within the reduced web section. The SHAP summary plot  
587 suggests that increasing  $A_a$ ,  $h_b$ , and  $t_{bf}$  generally leads to higher  $M_u$ , which is consistent with  
588 structural mechanics principles. The influence of connection type (e.g., “welded”) is moderate,  
589 indicating that while connection properties affect moment transfer, the primary governing factors  
590 are section dimensions. Features such as beam yield strength ( $f_{yn_{beam}}$ ), column elastic modulus  
591 ( $E_{col}$ ), and column length ( $L_c$ ) have minimal impact, reaffirming that local cross-sectional  
592 properties and geometry are the primary drivers of Ultimate Moment capacity [67].  
593



(a)



(b)



(c)

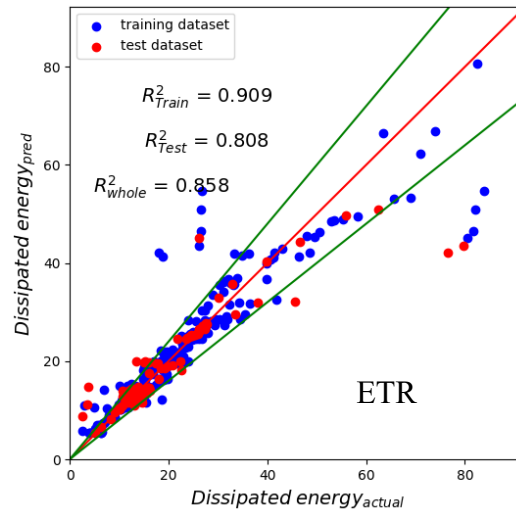
595 **Figure 8.** Performance of the optimum ML model in predicting the ultimate moment of RWS  
 596 connection; (a) Comparison of actual vs. predicted values; (b) SHAP summary plot of the  
 597 predictions; (c) Ranking of feature’s impact on the prediction model.

598

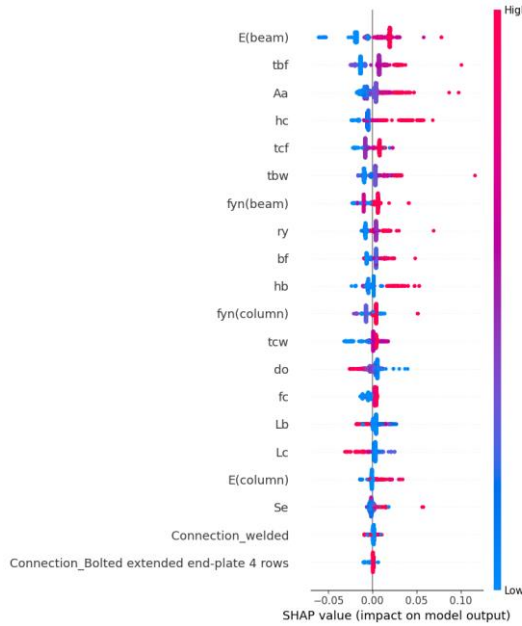
599 5.1.4. Dissipated Energy

600 The evaluation of machine learning models for predicting Dissipated Energy ( $E_d$ ) reveals  
 601 that while all three models exhibit reasonable accuracy, XGBoost outperforms the others in

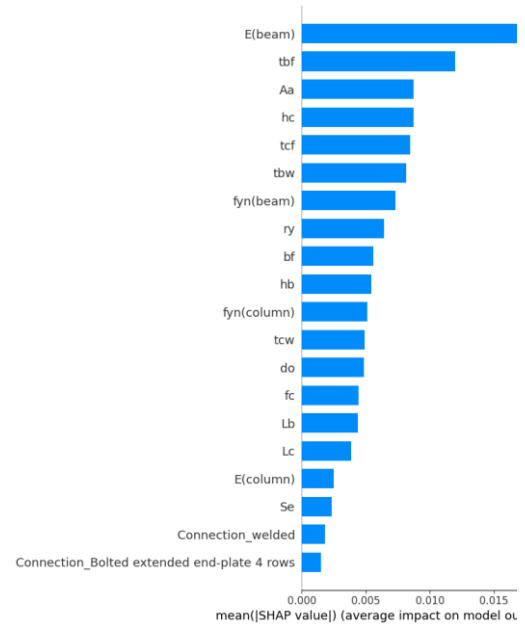
602 generalization, achieving an  $R^2$  of 0.929 on the training dataset, though its test  $R^2$  drops to 0.685,  
603 indicating potential overfitting or the inherent complexity of predicting energy dissipation. ETR  
604 performed slightly better in terms of test generalization ( $R^2 = 0.808$ ), while GTBR showed the  
605 lowest performance on the test set ( $R^2 = 0.698$ ). While XGBoost demonstrated superior  
606 predictive accuracy for most outputs, the Extra Trees Regressor provided a higher  $R^2$  value for  
607 energy dissipated ( $E_d$ ) on the testing dataset (0.808 vs. 0.685). This metric is particularly  
608 sensitive to local connection details and cyclic loading history, making its prediction more  
609 challenging. For subsequent optimization, the best-performing model for each output in the  
610 testing dataset was selected to ensure robust and objective-driven predictions. To further  
611 investigate the factors influencing dissipated energy predictions, SHAP analysis was performed  
612 on the optimum ML model as illustrated in Figure 9. The results highlight that beam elastic  
613 modulus ( $E_{beam}$ ) is the most dominant predictor, followed by flange thickness ( $t_{bf}$ ), cross-  
614 sectional area ( $A_a$ ), column height ( $h_c$ ), and column flange thickness ( $t_{cf}$ ). This indicates that  
615 energy dissipation is strongly influenced by the stiffness properties of the beam and column, as  
616 well as the overall section geometry, which govern plastic deformation capacity and hysteretic  
617 behavior.  
618



(a)



(b)



(c)

620 **Figure 9.** Performance of the optimum ML model in predicting the dissipated energy of RWS  
 621 connection; (a) Comparison of actual vs. predicted values; (b) SHAP summary plot of the  
 622 predictions; (c) Ranking of feature’s impact on the prediction model.

623

624 The SHAP summary plot further reveals that higher values of  $E_{beam}$  and  $t_{bf}$  correspond  
 625 to increased dissipated energy, which aligns with structural mechanics principles, as stiffer beams  
 626 and thicker flanges enhance plastic energy dissipation. Additionally, web thickness ( $t_{bw}$ ) and

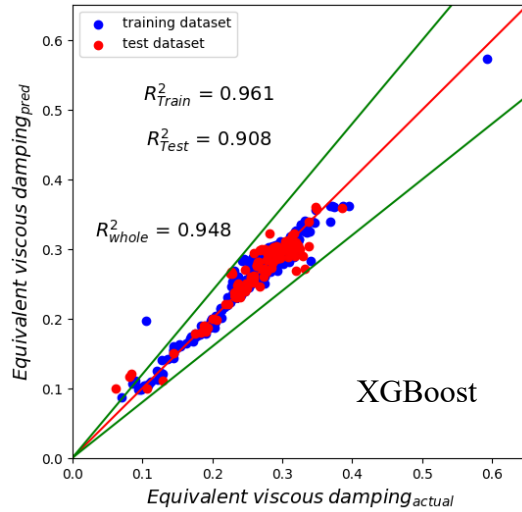
627 yield strength of the beam ( $f_{yn_{beam}}$ ) show moderate influence, suggesting that material strength  
628 also plays a crucial role. Interestingly, connection type (e.g., “Bolted extended end-plate 4 rows”)  
629 has a minor influence, indicating that while connections contribute to energy dissipation, the  
630 primary governing factors are the material and geometric properties of the beam and column  
631 rather than the connection detailing. Lower-ranked features such as column elastic modulus  
632 ( $E_{col}$ ) and column yield strength ( $f_{yn_{column}}$ ) exhibit minimal impact, reinforcing the notion that  
633 beam behavior is more critical than column properties in determining dissipated energy [68,69].

634 These findings highlight the complexity of modelling energy dissipation, as it is governed  
635 by non-linear interactions between material properties, section geometry, and plastic hinge  
636 formation. While XGBoost provides the most robust predictions, the SHAP analysis suggests  
637 that further refinement, possibly incorporating additional hysteresis-related parameters, could  
638 enhance the model’s predictive power.

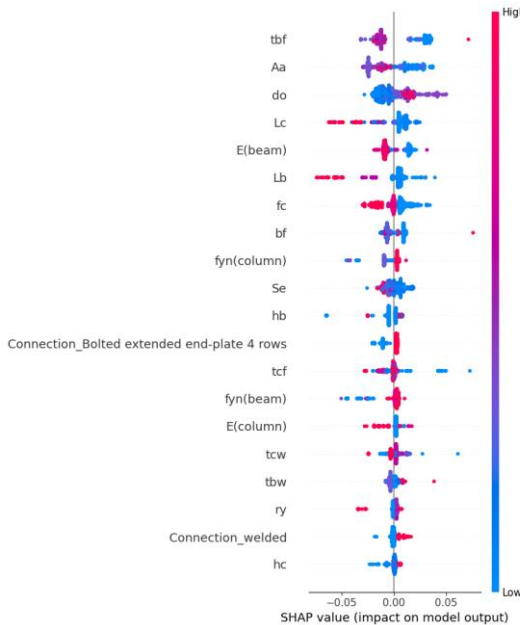
639

#### 640 5.1.5. Equivalent Viscous Damping

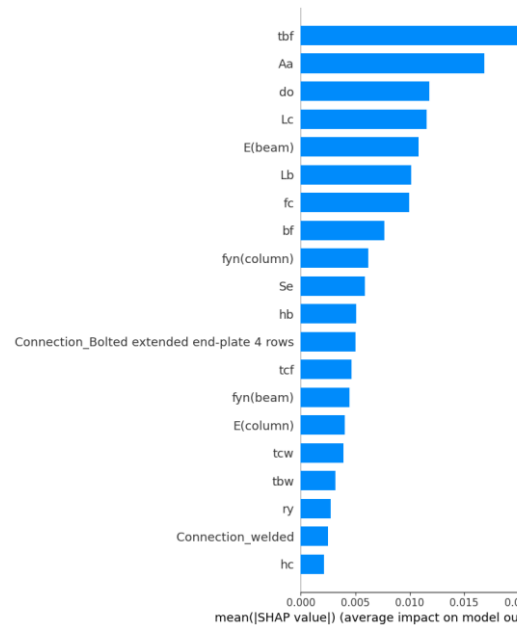
641 The ML models used to predict Equivalent Viscous Damping ( $\zeta_{eq}$ ) demonstrated high  
642 predictive accuracy, with XGBoost achieving the lowest test MAPE (4.216%) and the highest  
643  $R^2$ (0.908), indicating superior generalization. While ETR achieved the lowest training error  
644 (MAPE: 2.981%), its test error (MAPE: 4.343%) was slightly higher, suggesting some degree of  
645 overfitting, whereas GTBR maintained balanced performance with an  $R^2$  of 0.891, confirming  
646 its ability to capture the damping characteristics effectively. To better understand the influence  
647 of different features on  $\zeta_{eq}$ , SHAP analysis was conducted to interpret the optimum model’s  
648 predictions as shown in Figure 10. The results indicate that flange thickness ( $t_{bf}$ ) and cross-  
649 sectional area ( $A_a$ ) are the most dominant predictors, highlighting their role in influencing  
650 damping behavior by affecting energy dissipation and stiffness. The diameter of the opening ( $do$ )  
651 and column length ( $L_c$ ) also have a significant impact, suggesting that the presence of web  
652 openings and overall beam-column geometry contribute to damping capacity. The elastic  
653 modulus of the beam ( $E_{beam}$ ) and beam length ( $L_b$ ) further influence damping, reinforcing the  
654 notion that stiffness properties and beam flexibility contribute to energy dissipation mechanisms.



(a)



(b)



(c)

655 **Figure 10.** Performance of the optimum ML model in predicting the equivalent viscous damping  
 656 of RWS connection; (a) Comparison of actual vs. predicted values; (b) SHAP summary plot of the  
 657 predictions; (c) Ranking of feature’s impact on the prediction model.

658

659 The SHAP summary plot further reveals that higher values of  $t_{bf}$ ,  $A_a$ , and  $do$  generally  
 660 lead to increased  $\zeta_{eq}$ , which is consistent with structural behavior where larger cross-sections  
 661 and web openings influence damping capacity by modifying deformation characteristics.  
 662 Additionally, the connection type (“Bolted extended end-plate 4 rows”) shows moderate

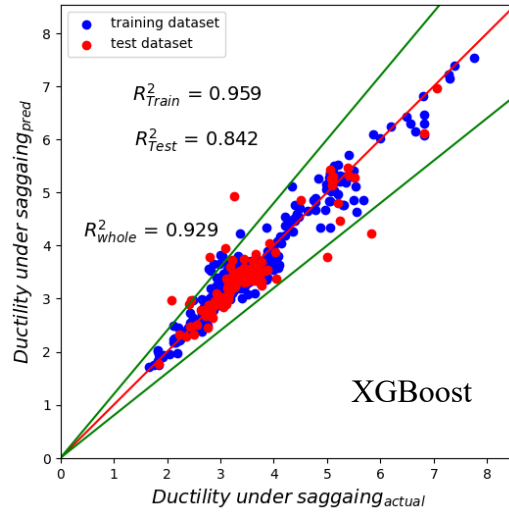
663 influence, indicating that while connection configuration affects damping, material and  
664 geometric factors are the primary determinants. Features such as column flange thickness ( $t_{cf}$ ),  
665 beam yield strength ( $f_{yn_{beam}}$ ), and column elastic modulus ( $E_{col}$ ) have a lower impact,  
666 suggesting that the energy dissipation mechanism is predominantly governed by local section  
667 properties rather than global material strength. Interestingly, welded connections and column  
668 height ( $h_c$ ) exhibit minimal influence, implying that while these factors contribute to overall  
669 structural behavior, they play a less significant role in damping capacity [70,71].

670 These findings reinforce the physical consistency of the ML model, demonstrating that  
671 XGBoost effectively captures the relationship between stiffness, energy dissipation, and damping  
672 behavior. The SHAP analysis validates the importance of beam and web geometry, stiffness  
673 properties, and connection details in determining  $\zeta_{eq}$ .

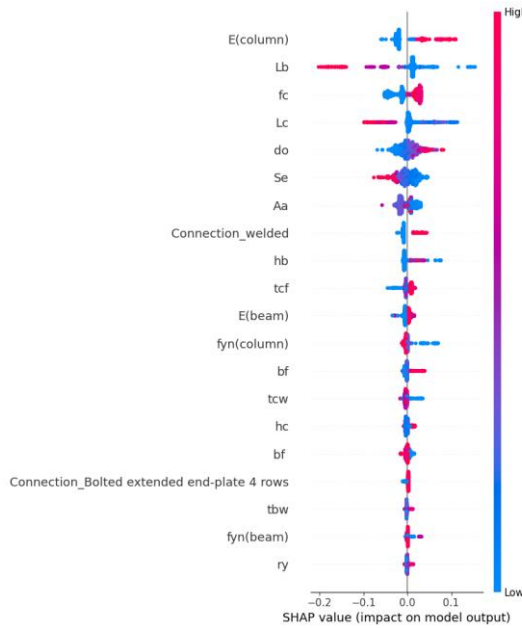
674

#### 675 5.1.6. Ductility Under Sagging

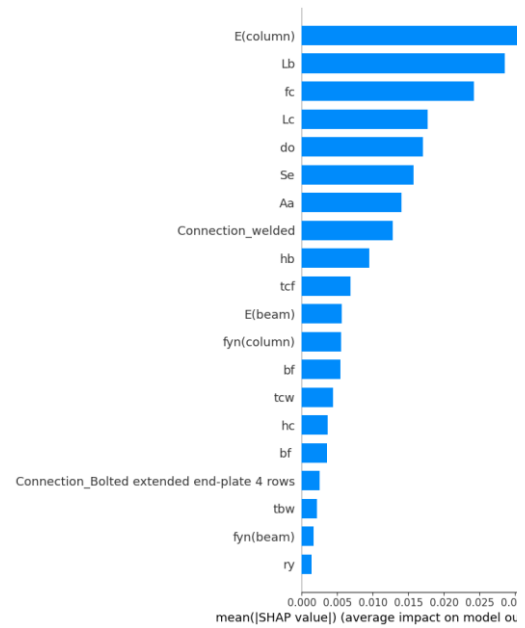
676 The prediction of Ductility Under Sagging ( $\theta_u/\theta_y$  +ve) using ML models demonstrates  
677 that XGBoost achieves the best generalization performance, with the lowest test MAPE (5.099%)  
678 and the highest  $R^2$  (0.842), indicating its strong capability to capture the nonlinear relationships  
679 governing ductility behavior. ETR exhibited the lowest training error (MAPE: 2.55%), but its  
680 test MAPE (5.76%) suggests slight overfitting. Meanwhile, GTBR showed a higher test MAPE  
681 (6.574%), which indicates a moderate generalization capability but a slight tendency to  
682 underperform in unseen data. The SHAP analysis was conducted to further interpret the feature  
683 contributions to model predictions as shown in Figure 11. The results reveal that column elastic  
684 modulus ( $E_{column}$ ) is the most influential predictor, followed by beam length ( $L_b$ ), concrete  
685 compressive strength ( $f_c$ ), column length ( $L_c$ ), and the diameter of the web opening ( $d_o$ ). These  
686 features significantly impact ductility by influencing deformation capacity, material stiffness,  
687 and load redistribution mechanisms.



(a)



(b)



(c)

688 **Figure 11.** Performance of the optimum ML model in predicting the ductility under sagging of  
 689 RWS connection; (a) Comparison of actual vs. predicted values; (b) SHAP summary plot of the  
 690 predictions; (c) Ranking of feature's impact on the prediction model.

691

692 The SHAP summary plot indicates that higher values of  $E_{column}$  and  $L_b$  are associated  
 693 with increased ductility, aligning with structural mechanics principles where greater column  
 694 stiffness and longer beams enhance deformation capacity under sagging moments. The presence  
 695 of web openings ( $d_o$ ) plays a notable role, as it affects local buckling and energy dissipation

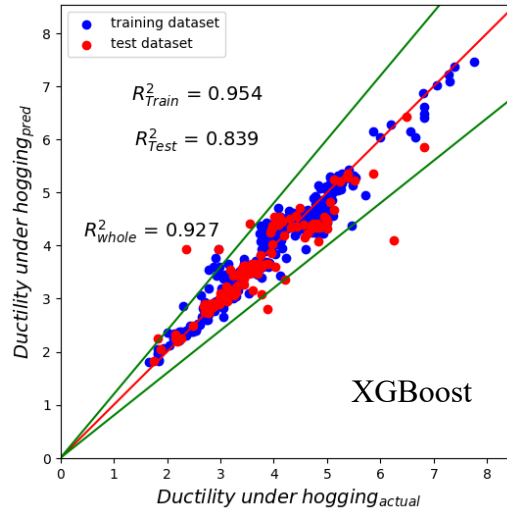
696 mechanisms. The size and location of web opening ( $d_o$  and  $S_e$ ) also exhibit moderate importance,  
697 reinforcing their role in determining the plastic rotation capacity. Interestingly, connection type  
698 (e.g., “welded” or “Bolted extended end-plate 4 rows”) has a measurable impact, though it is not  
699 as dominant as material and geometric factors, suggesting that while connection stiffness  
700 influences ductility, the overall structural configuration and material behavior are the primary  
701 drivers. Features such as beam flange thickness ( $t_{bf}$ ), web thickness ( $t_{bw}$ ), and beam yield  
702 strength ( $f_{yn_{beam}}$ ) show a lower contribution, indicating that local cross-sectional parameters  
703 contribute less significantly to ductility compared to global stiffness and geometry effects  
704 [65,72].

705 These findings suggest that ductility under sagging moments is primarily controlled by  
706 column stiffness, beam length, and web opening effects, while connection type and beam cross-  
707 section play a secondary role.

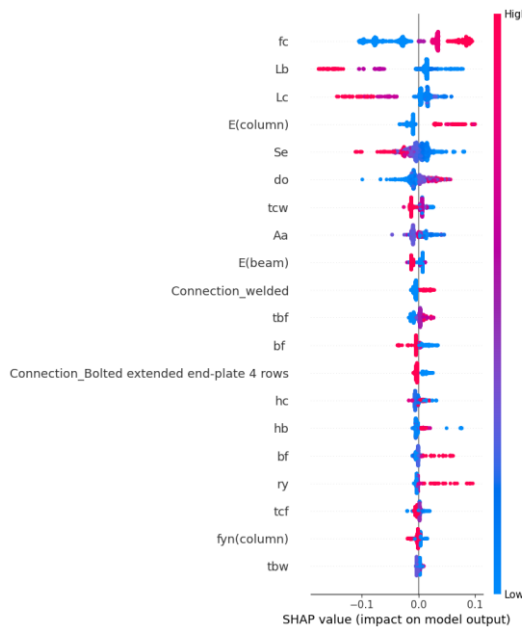
708

#### 709 5.1.7. Ductility Under Hogging

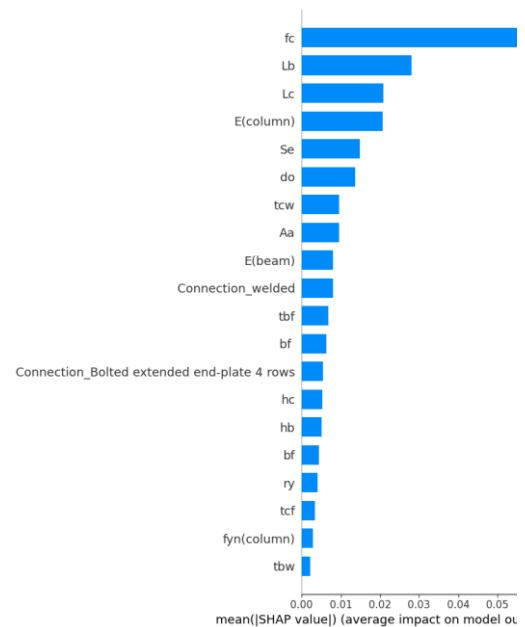
710 The prediction of Ductility Under Hogging ( $\theta_u/\theta_y$  -ve) using machine learning models  
711 shows that XGBoost provides the most accurate generalization, achieving the highest test  $R^2$   
712 (0.839) and the lowest test MAPE (5.711%), suggesting its effectiveness in capturing the  
713 complex relationships governing ductility behavior under hogging moments. ETR exhibited the  
714 lowest training error (MAPE: 4.051%), but its test error (MAPE: 6.386%) was slightly higher,  
715 indicating some overfitting, whereas GTBR maintained relatively balanced performance (test  
716 MAPE: 6.145%). To gain further insight into the model’s decision-making process, SHAP  
717 analysis was performed to quantify feature importance and their impact on predictions as shown  
718 in Figure 12. The results indicate that concrete compressive strength ( $f_c$ ) is the most influential  
719 predictor, followed by beam length ( $L_b$ ), column length ( $L_c$ ), column elastic modulus ( $E_{column}$ ),  
720 and section modulus ( $Se$ ). These features significantly affect ductility by governing the stiffness,  
721 load redistribution, and deformation capacity of the system.



(a)



(b)



(c)

722 **Figure 12.** Performance of the optimum ML model in predicting the ductility under hogging of  
 723 RWS connection; (a) Comparison of actual vs. predicted values; (b) SHAP summary plot of the  
 724 predictions; (c) Ranking of feature's impact on the prediction model.

725

726 The SHAP summary plot suggests that higher values of  $f_c$ ,  $L_b$ , and  $E_{column}$  are positively  
 727 correlated with increased ductility, which is consistent with structural mechanics principles,  
 728 where greater stiffness, increased member length, and improved concrete strength contribute to  
 729 enhanced deformation capacity under hogging moments. Additionally, the diameter of web

730 openings ( $d_o$ ) and total cross-sectional area ( $A_a$ ) exhibit moderate influence, indicating that web  
731 openings and section geometry affect the plastic hinge formation and rotational capacity of the  
732 connection. Interestingly, connection type (e.g., “welded” or “Bolted extended end-plate 4 rows”)  
733 has a measurable impact, suggesting that while connection detailing contributes to ductility, the  
734 primary governing factors are material properties and global geometry. Lower-ranked features  
735 such as flange thickness ( $t_{bf}$ ), web thickness ( $t_{bw}$ ), and column yield strength ( $f_{yn_{column}}$ )  
736 exhibit minimal influence, reinforcing that ductility is predominantly influenced by stiffness and  
737 member length rather than local cross-sectional properties [73].

738         These findings emphasize that ductility under hogging moments is primarily controlled  
739 by material strength (especially concrete compressive strength), beam and column stiffness, and  
740 geometric properties, while connection characteristics play a secondary role.

741

## 742         5.2. Multi-objective optimisation

743         Figure 13 illustrates the results of the multi-objective optimisation process applied to  
744 RWS connections, considering seven mechanical performance criteria—Yield Moment,  
745 Maximum Moment, Ultimate Moment, Dissipated Energy, Equivalent Viscous Damping,  
746 Ductility Under Sagging, and Ductility Under Hogging—along with total embodied carbon (EC)  
747 reduction as a sustainability objective. The figure presents a pairwise correlation matrix between  
748 these variables, showing the trade-offs and interactions between different performance metrics.



749

750 **Figure 13.** Multi-objective optimisation for RWS connections with 7 output variables and total  
 751 embodied carbon reduction.

752

753 The scatter plots compare the optimized solutions (red) with the real dataset (blue),  
 754 providing insights into the feasible design space and the diversity of the Pareto-optimal solutions.  
 755 Notably, strong positive correlations are observed among Yield Moment, Maximum Moment,  
 756 and Ultimate Moment, indicating that increasing the flexural strength of RWS connections tends

757 to improve all three moment capacities simultaneously. However, trade-offs emerge between  
758 mechanical performance and sustainability objectives, where higher structural strength may  
759 result in an increase in embodied carbon, highlighting the necessity of balancing performance  
760 with environmental impact.

761 For Dissipated Energy and Equivalent Viscous Damping, the results suggest a nonlinear  
762 relationship with other structural properties, reinforcing the complexity of energy dissipation  
763 mechanisms in RWS connections. The distributions of Ductility Under Sagging and Ductility  
764 Under Hogging indicate that higher ductility values are generally associated with increased  
765 energy dissipation but may also contribute to greater embodied carbon, presenting a critical  
766 design trade-off.

767 It is worth noting that, a direct comparison with traditional RWS design formulas is  
768 limited, as such methods generally predict a single property (e.g., moment capacity). In contrast,  
769 the proposed framework simultaneously predicts eight properties and incorporates multi-  
770 objective optimisation, enabling a broader and more integrated design capability.

771 The Pareto-optimal solutions generated by NSGA-II provide a well-distributed set of  
772 optimized designs, enabling decision-makers to select optimal configurations based on structural  
773 performance priorities and sustainability constraints. These results underscore the effectiveness  
774 of the multi-objective optimisation framework in guiding the design of RWS connections,  
775 offering valuable insights into the interplay between mechanical properties and carbon footprint  
776 reduction. The Pareto-optimal solutions are directly integrated in the user-friendly online  
777 interface.

778

#### 779 5.4. User-friendly interface

780 A user-friendly interface was developed and deployed online via Hugging Face at the  
781 following link ([https://huggingface.co/spaces/MohamedRabie26/RWS\\_connections](https://huggingface.co/spaces/MohamedRabie26/RWS_connections)). This tool  
782 provides users with two functionalities: (1) Predictions based on user-defined input parameters  
783 and (2) Multi-objective optimisation, where users can specify one objective output, and the tool  
784 returns the corresponding optimal input parameters along with the six remaining mechanical  
785 properties and the total embodied carbon (EC) reduction. The optimization is based on the nearest  
786 Pareto-optimal solution generated from the multi-objective optimization process, ensuring that

787 the suggested design configurations maintain a balance between performance and sustainability.  
 788 The predictions are generated using the optimal ML model identified in this study, ensuring high  
 789 accuracy and reliability. The interface includes an intuitive slider-based input system, allowing  
 790 users to select values within the trained data range specified in Table 2, ensuring the generated  
 791 outputs remain within the model’s predictive capabilities for reliability and practicality.  
 792 Additionally, the tool provides Pareto-optimal solutions, offering valuable insights into the trade-  
 793 offs between different performance metrics and sustainability objectives, as illustrated in Figure  
 794 14. The developed interface is intended for interpolative use within the parameter space of the  
 795 training data, ensuring reliable predictions for configurations represented in the database. It is  
 796 worth mentioning that predictions outside this range may carry higher uncertainty and are beyond  
 797 the tool’s intended scope.

(a)

(b)

**Figure 14.** Composite RWS connection online interface; (a) Mechanical and ductility properties prediction; (b) Multi-objective optimisation with for the output variables and corresponding input variables.

798

799 Furthermore, this tool can be integrated into ML workflows via the Hugging Face API,  
 800 facilitating its application in structural engineering optimization and sustainable design  
 801 initiatives. This capability supports researchers and industry professionals in making data-driven  
 802 decisions, enhancing the design efficiency of RWS connections, and promoting the development  
 803 of structurally optimized and environmentally sustainable solutions.

804

## 805 6. Concluding Remarks

806 This study developed a machine learning-based framework for predicting and optimizing  
 807 the mechanical performance and embodied carbon reduction of RWS connections. Three  
 808 ensemble models namely, Extra Trees Regressor (ETR), Gradient Tree Boosting (GTBR), and  
 809 Extreme Gradient Boosting (XGBoost) were evaluated, with XGBoost demonstrating superior  
 810 generalization across most outputs. The SHAP analysis provided interpretability, confirming that  
 811 key structural parameters, such as cross-sectional properties, material stiffness, and connection

812 type, significantly influence the predicted responses. A multi-objective optimisation approach  
813 using NSGA-II was implemented to explore trade-offs between mechanical performance and  
814 embodied carbon reduction, generating Pareto-optimal solutions for informed decision-making.

815 The key findings are:

- 816 • Machine learning predictions confirmed that XGBoost consistently achieved the highest  
817 generalization performance, particularly for Yield Moment, Maximum Moment, and  
818 Ductility predictions, with the lowest test MAPE and highest  $R^2$ .
- 819 • SHAP analysis revealed that cross-sectional properties, particularly flange thickness ( $t_{bf}$ ),  
820 cross-sectional area ( $A_a$ ), and beam height ( $h_b$ ), were the most influential features for  
821 predicting moment capacities.
- 822 • Ductility predictions were primarily governed by material properties and member stiffness,  
823 with concrete compressive strength ( $f_c$ ), beam length ( $L_b$ ), and column elastic modulus  
824 ( $E_{column}$ ) playing a dominant role in both sagging and hogging ductility.
- 825 • Multi-objective optimization highlighted trade-offs between structural performance and  
826 sustainability, demonstrating that higher moment capacities and ductility often come at the  
827 cost of increased embodied carbon, requiring a balance in design selection.

828 Additionally, a user-friendly interface was developed and deployed on Hugging Face, enabling  
829 users to make predictions and retrieve optimized design parameters based on the nearest Pareto-  
830 optimal solutions. This tool facilitates efficient and sustainable design exploration by balancing  
831 structural performance and environmental impact, though it is intended specifically for  
832 preliminary design guidance and must be utilized alongside official structural standards for final  
833 practical verification. The findings demonstrate the potential of AI-driven decision support  
834 systems in structural engineering, paving the way for more data-driven, optimized, and  
835 sustainable connection designs.

836

837

838 **Author Contributions**

839 **Mohamed Rabie:** Conceptualization, Formal analysis, Investigation, Methodology,  
840 Visualization, Software, Writing – original draft, Writing – review & editing. **Fahad Falah**  
841 **Almutairi:** Conceptualization, Investigation, Methodology, Visualization, Data curation, Writing  
842 – original draft, Writing – review & editing. **Konstantinos Daniel Tsavdaridis:**  
843 Conceptualization, Supervision, Validation, Writing – review & editing. **Ibrahim G. Shaaban:**  
844 Conceptualization, Supervision, Validation, Writing – review & editing.

845

846 All authors have read and agreed to the published version of the manuscript.

847 **Conflicts of Interest**

848 The authors declare no conflict of interest.

849 **Acknowledgment**

850 This work was partially funded by the University of West London Vice Chancellor's  
851 Scholarship awarded to the first author.

852 **Data Availability Statement**

853 The compiled database of RWS connections is openly available in a public repository to  
854 facilitate reproducibility and further research (Mendeley Data,  
855 <https://data.mendeley.com/datasets/66s35tgvd3/1>).

856

- 858 [1] C.-M. Uang, Q.-S. “Kent” Yu, S. Noel, J. Gross, Cyclic testing of steel moment connections  
859 rehabilitated with RBS or welded haunch, *J. Struct. Eng.* 126 (2000) 57–68.
- 860 [2] X. Zhang, J.M. Ricles, L.-W. Lu, J.W. Fisher, Development of seismic guidelines for deep-  
861 column steel moment connections, (2004).
- 862 [3] M. D’Aniello, R. Tartaglia, R. Landolfo, J.-P. Jaspart, J.-F. Demonceau, Seismic pre-  
863 qualification tests of EC8-compliant external extended stiffened end-plate beam-to-column  
864 joints, *Eng. Struct.* 291 (2023) 116386.
- 865 [4] AISC, China, Global Warming and Hot-Rolled Structural Steel Sections., American Steel  
866 Institute, White paper F157-18., 2018.
- 867 [5] A. Mullholland, C. Ackerman, P. Astle, M. Drewniok, A. Dunster, A. Hibbert, R. Inman, R.  
868 Kershaw, B. Martin, C. McCague, Low Carbon Concrete Routemap. Setting the Agenda for  
869 a Path to Net Zero, (2022).
- 870 [6] F.F. Almutairi, K.D. Tsavdaridis, Capacity design assessment of composite reduced web  
871 section (RWS) connections, *Eng. Struct.* 316 (2024) 118558.  
872 <https://doi.org/10.1016/j.engstruct.2024.118558>.
- 873 [7] S. Erfani, V. Akrami, Increasing Seismic Energy Dissipation of Steel Moment Frames Using  
874 Reduced Web Section (RWS) Connection, *J. Earthq. Eng.* 21 (2017) 1090–1112.
- 875 [8] F.F. Almutairi, K.D. Tsavdaridis, A. Alonso-Rodríguez, I. Hajirasouliha, Experimental  
876 investigation using demountable steel-concrete composite reduced web section (RWS)  
877 connections under cyclic loads, *Bull. Earthq. Eng.* 22 (2024) 1081–1110.  
878 <https://doi.org/10.1007/s10518-023-01802-y>.
- 879 [9] S. Lin, H. Qiao, J. Wang, J. Shi, Y. Chen, Anti-collapse performance of steel frames with  
880 RWS connections under a column removal scenario, *Eng. Struct.* 227 (2021) 111495.
- 881 [10] K.D. Tsavdaridis, C.K. Lau, A. Alonso-Rodríguez, Experimental behaviour of non-seismical  
882 RWS connections with perforated beams under cyclic actions, *J. Constr. Steel Res.* 183  
883 (2021) 106756.
- 884 [11] H. Nazaralizadeh, H. Ronagh, P. Memarzadeh, F. Behnamfar, Cyclic performance of bolted  
885 end-plate RWS connection with vertical-slits, *J. Constr. Steel Res.* 173 (2020) 106236.
- 886 [12] K.D. Tsavdaridis, C. D’Mello, Vierendeel bending study of perforated steel beams with  
887 various novel web opening shapes through nonlinear finite-element analyses, *J. Struct. Eng.*  
888 138 (2012) 1214–1230.
- 889 [13] K.D. Tsavdaridis, F. Faghieh, N. Nikitas, Assessment of perforated steel beam-to-column  
890 connections subjected to cyclic loading, *J. Earthq. Eng.* 18 (2014) 1302–1325.
- 891 [14] V. Akrami, S. Erfani, Effect of local web buckling on the cyclic behavior of reduced web  
892 beam sections (RWBS), *Steel Compos. Struct.* 18 (2015) 641–657.
- 893 [15] K.D. Tsavdaridis, C. Pilbin, C.K. Lau, FE parametric study of RWS/WUF-B moment  
894 connections with elliptically-based beam web openings under monotonic and cyclic loading,  
895 *Int. J. Steel Struct.* 17 (2017) 677–694.
- 896 [16] S. Erfani, V. Akrami, A. Mohammad-nejad, Lateral load resisting behavior of steel moment  
897 frames with reduced web section (RWS) beams, in: *Structures*, Elsevier, 2020: pp. 251–265.
- 898 [17] S. Erfani, V. Akrami, A Nonlinear Macro-model for Numerical Simulation of Perforated  
899 Steel Beams, *Int. J. Steel Struct.* (2019) 1–19.
- 900 [18] K. Boushehri, K.D. Tsavdaridis, G. Cai, Seismic behaviour of RWS moment connections to

- 901 deep columns with European sections, *J. Constr. Steel Res.* 161 (2019) 416–435.
- 902 [19] M.A. Shaheen, K.D. Tsavdaridis, S. Yamada, Comprehensive FE Study of the Hysteretic  
903 Behaviour of Steel-Concrete Composite and Non-Composite RWS Beam-to-Column  
904 Connections, *J. Struct. Eng.* (2018).
- 905 [20] F.F. Almutairi, K.D. Tsavdaridis, A. Alonso Rodriguez, P.G. Asteris, M.E. Lemonis,  
906 Hysteretic Behaviour of Composite Reduced Web Section (RWS) Connections for Seismic  
907 Applications, *J. Earthq. Eng.* 28 (2023) 349–384.  
908 <https://doi.org/10.1080/13632469.2023.2204172>.
- 909 [21] A.M. Tabar, A. Alonso-Rodriguez, K. Daniel Tsavdaridis, Building Retrofit with Reduced  
910 Web (RWS) and Beam (RBS) Section Limited-Ductility Connections, *J. Constr. Steel Res.*  
911 (2022).
- 912 [22] A. Khoshkroodi, H.P. Sani, M. Aajami, Stacking Ensemble-Based Machine Learning Model  
913 for Predicting Deterioration Components of Steel W-Section Beams, *Buildings* (2024).  
914 <https://doi.org/10.3390/buildings14010240>.
- 915 [23] K. Cheng, Z. Lu, Structural reliability analysis based on ensemble learning of surrogate  
916 models, *Struct. Saf.* (2020). <https://doi.org/10.1016/j.strusafe.2019.101905>.
- 917 [24] R.O. Hamburger, J.O. Malley, Seismic design of steel special moment frames, US  
918 Department of Commerce, National Institute of Standards and Technology ..., 2016.
- 919 [25] G. Georgiou, A. Elkady, ANN-Based Model for Predicting the Nonlinear Response of Flush  
920 Endplate Connections, *J. Struct. Eng.* 150 (2024) 4024034.
- 921 [26] F.P.V. Ferreira, R. Shamass, V. Limbachiya, K.D. Tsavdaridis, C.H. Martins, Lateral–  
922 torsional buckling resistance prediction model for steel cellular beams generated by Artificial  
923 Neural Networks (ANN), *Thin-Walled Struct.* 170 (2022) 108592.
- 924 [27] V.V. Degtyarev, K.D. Tsavdaridis, Buckling and ultimate load prediction models for  
925 perforated steel beams using machine learning algorithms, *J. Build. Eng.* 51 (2022) 104316.
- 926 [28] M. Rabie, I.G. Shaaban, Glass fibre concrete: Experimental investigation and predictive  
927 modeling using advanced machine learning with an interactive online interface, *Constr.*  
928 *Build. Mater.* 472 (2025) 140951. <https://doi.org/10.1016/j.conbuildmat.2025.140951>.
- 929 [29] T.G. Wakjira, M. Ibrahim, U. Ebead, M.S. Alam, Explainable machine learning model and  
930 reliability analysis for flexural capacity prediction of RC beams strengthened in flexure with  
931 FRCM, *Eng. Struct.* 255 (2022) 113903. <https://doi.org/10.1016/j.engstruct.2022.113903>.
- 932 [30] T.G. Wakjira, A.A. Kutty, M.S. Alam, A novel framework for developing environmentally  
933 sustainable and cost-effective ultra-high-performance concrete (UHPC) using advanced  
934 machine learning and multi-objective optimization techniques, *Constr. Build. Mater.* 416  
935 (2024) 135114. <https://doi.org/10.1016/j.conbuildmat.2024.135114>.
- 936 [31] T.G. Wakjira, M.S. Alam, Peak and ultimate stress-strain model of confined ultra-high-  
937 performance concrete (UHPC) using hybrid machine learning model with conditional tabular  
938 generative adversarial network, *Appl. Soft Comput.* 154 (2024) 111353.  
939 <https://doi.org/10.1016/j.asoc.2024.111353>.
- 940 [32] C. Li, H. Li, X. Chen, A framework for fast estimation of structural seismic responses using  
941 ensemble machine learning model, *Smart Struct Syst* 28 (2021) 425–441.
- 942 [33] T. Vlasenko, T. Hutsol, V. Vlasovets, S. Glowacki, T. Nurek, I. Horetska, S. Kukharets, Y.  
943 Firman, O. Bilovod, Ensemble learning based sustainable approach to rebuilding metal  
944 structures prediction, *Sci. Rep.* 15 (2025) 1210.
- 945 [34] C. Molnar, *Interpretable machine learning*, Lulu. com, 2020.

- 946 [35] S.M. Lundberg, S.-I. Lee, A unified approach to interpreting model predictions, *Adv. Neural*  
947 *Inf. Process. Syst.* 30 (2017).
- 948 [36] O. Loyola-González, Black-Box vs. White-Box: Understanding Their Advantages and  
949 Weaknesses From a Practical Point of View, *IEEE Access* 7 (2019) 154096–154113.  
950 <https://doi.org/10.1109/ACCESS.2019.2949286>.
- 951 [37] D.D. Tingley, B. Davison, Developing an LCA methodology to account for the  
952 environmental benefits of design for deconstruction, *Build. Environ.* 57 (2012) 387–395.
- 953 [38] O.O. Akinade, L.O. Oyedele, S.O. Ajayi, M. Bilal, H.A. Alaka, H.A. Owolabi, S.A. Bello,  
954 B.E. Jaiyeoba, K.O. Kadiri, Design for Deconstruction (DfD): Critical success factors for  
955 diverting end-of-life waste from landfills, *Waste Manag.* 60 (2017) 3–13.
- 956 [39] B. Guo, J.T. Wang, T. Liang, Z. Bao, Study on seismic performance of a new type energy  
957 dissipation steel moment frames, in: *Appl. Mech. Mater.*, Trans Tech Publ, 2011: pp. 764–  
958 770.
- 959 [40] B. Li, Q. Yang, N. Yang, An investigation on aseismic connection with opening in beam web  
960 in steel moment frames, *Adv. Struct. Eng.* 14 (2011) 575–587.
- 961 [41] K.D. Tsavdaridis, T. Papadopoulos, A FE parametric study of RWS beam-to-column bolted  
962 connections with cellular beams, *J. Constr. Steel Res.* 116 (2016) 92–113.
- 963 [42] M. Shin, S.-P. Kim, A. Halterman, M. Aschheim, Seismic toughness and failure mechanisms  
964 of reduced web-section beams: Phase 2 tests, *Eng. Struct.* 141 (2017) 607–623.
- 965 [43] X. Zhang, S. Zheng, X. Zhao, Seismic performance of steel beam-to-column moment  
966 connections with different structural forms, *J. Constr. Steel Res.* 158 (2019) 130–142.
- 967 [44] Q. Xu, H. Chen, W. Li, S. Zheng, X. Zhang, Experimental investigation on seismic behavior  
968 of steel welded connections considering the influence of structural forms, *Eng. Fail. Anal.*  
969 139 (2022) 106499.
- 970 [45] M.H. Nguyen, H.-V.T. Mai, S.H. Trinh, H.-B. Ly, A comparative assessment of tree-based  
971 predictive models to estimate geopolymer concrete compressive strength, *Neural Comput.*  
972 *Appl.* 35 (2023) 6569–6588. <https://doi.org/10.1007/s00521-022-08042-2>.
- 973 [46] U. Sharma, N. Gupta, M. Verma, Prediction of compressive strength of GGBFS and Flyash-  
974 based geopolymer composite by linear regression, lasso regression, and ridge regression,  
975 *Asian J. Civ. Eng.* 24 (2023) 3399–3411. <https://doi.org/10.1007/s42107-023-00721-2>.
- 976 [47] M. Anjum, K. Khan, W. Ahmad, A. Ahmad, M.N. Amin, A. Nafees, Application of Ensemble  
977 Machine Learning Methods to Estimate the Compressive Strength of Fiber-Reinforced Nano-  
978 Silica Modified Concrete, *Polymers* 14 (2022) 3906.  
979 <https://doi.org/10.3390/polym14183906>.
- 980 [48] M.S. Rana, M.M. Hossain, F. Li, Comparative analysis of machine learning models for  
981 predicting the compressive strength of ultra-high-performance steel fiber reinforced concrete,  
982 *J. Eng. Res.* (2025). <https://doi.org/10.1016/j.jer.2025.01.004>.
- 983 [49] M. Rabie, M. Ibrahim, U. Ebead, I.G. Shaaban, Optimising sustainable alkali-activated  
984 mortar: experimental work and machine learning predictions, *Proc. Inst. Civ. Eng. - Struct.*  
985 *Build.* 178 (2025) 828–850. <https://doi.org/10.1680/jstbu.25.00036>.
- 986 [50] P. Geurts, D. Ernst, L. Wehenkel, Extremely randomized trees, *Mach. Learn.* 63 (2006) 3–  
987 42.
- 988 [51] D. Kocev, M. Ceci, Ensembles of Extremely Randomized Trees for Multi-target Regression,  
989 (2015) 86–100. [https://doi.org/10.1007/978-3-319-24282-8\\_9](https://doi.org/10.1007/978-3-319-24282-8_9).
- 990 [52] T. Hastie, R. Tibshirani, J. Friedman, *The Elements of Statistical Learning*, Springer, New

- 991 York, NY, 2009. <https://doi.org/10.1007/978-0-387-84858-7>.
- 992 [53] J.H. Friedman, Greedy function approximation: a gradient boosting machine, *Ann. Stat.*  
993 (2001) 1189–1232.
- 994 [54] T. Chen, C. Guestrin, XGBoost: A Scalable Tree Boosting System, in: *Proc. 22nd ACM*  
995 *SIGKDD Int. Conf. Knowl. Discov. Data Min.*, 2016: pp. 785–794.  
996 <https://doi.org/10.1145/2939672.2939785>.
- 997 [55] T. Hastie, R. Tibshirani, J. Friedman, Ensemble Learning, in: T. Hastie, R. Tibshirani, J.  
998 Friedman (Eds.), *Elem. Stat. Learn. Data Min. Inference Predict.*, Springer, New York, NY,  
999 2009: pp. 605–624. [https://doi.org/10.1007/978-0-387-84858-7\\_16](https://doi.org/10.1007/978-0-387-84858-7_16).
- 1000 [56] C. Cakiroglu, M. Shahjalal, K. Islam, S.M.F. Mahmood, A.H.M.M. Billah, M.L. Nehdi,  
1001 Explainable ensemble learning data-driven modeling of mechanical properties of fiber-  
1002 reinforced rubberized recycled aggregate concrete, *J. Build. Eng.* 76 (2023) 107279.  
1003 <https://doi.org/10.1016/J.JOBE.2023.107279>.
- 1004 [57] K. Deb, A. Pratap, S. Agarwal, T. Meyarivan, A fast and elitist multiobjective genetic  
1005 algorithm: NSGA-II, *IEEE Trans. Evol. Comput.* 6 (2002) 182–197.  
1006 <https://doi.org/10.1109/4235.996017>.
- 1007 [58] J. Orr, O. Gibbons, W. Arnold, A brief guide to calculating embodied carbon, *Struct. Eng.* 98  
1008 (2020) 22–27. <https://doi.org/10.56330/JZNX5709>.
- 1009 [59] British Steel, Environmental Product Declaration (EPD) Report of Steel Rails and Sections  
1010 (including semi-finished long products), BRC Limited, Gwent, 2020.  
1011 <https://britishsteel.co.uk/who-we-are/sustainability/>.
- 1012 [60] S.E.P. Book, A brief guide to calculating embodied carbon, (n.d.).
- 1013 [61] M. Rabie, M.R. Irshidat, N. Al-Nuaimi, Ambient and Heat-Cured Geopolymer Composites:  
1014 mix design optimization and life cycle assessment, *Sustainability* 14 (2022) 4942.
- 1015 [62] M.R. Irshidat, N. Al-Nuaimi, W. Ahmed, M. Rabie, Feasibility of recycling waste carbon  
1016 black in cement mortar production: environmental life cycle assessment and performance  
1017 evaluation, *Constr. Build. Mater.* 296 (2021) 123740.
- 1018 [63] T. Akiba, S. Sano, T. Yanase, T. Ohta, M. Koyama, Optuna: A Next-generation  
1019 Hyperparameter Optimization Framework, in: *Proc. 25th ACM SIGKDD Int. Conf. Knowl.*  
1020 *Discov. Data Min.*, 2019.
- 1021 [64] L.E. Curtis, T.M. Murray, Column flange strength at moment end-plate connections, *Eng. J.*  
1022 26 (1989) 41–50.
- 1023 [65] E.A. Elhout, Effect of Beam-Column Connection Types on the Response Modification  
1024 Factors of Steel Frames, *Int. J. Steel Struct.* 24 (2024) 132–143.  
1025 <https://doi.org/10.1007/s13296-023-00805-4>.
- 1026 [66] J.E. Rodgers, S.A. Mahin, Effects of connection deformation softening on behavior of steel  
1027 moment frames subjected to earthquakes, *Int. J. Steel Struct.* 11 (2011) 29–37.  
1028 <https://doi.org/10.1007/S13296-011-1003-9>.
- 1029 [67] J.R. Joshi, J. Huang, Numerical Study of HSS-to-HSS Moment Connections Subjected to  
1030 Out-of-Plane Loading: Effect of Connection Eccentricity, *Int. J. Civ. Infrastruct.* 6 (2023)  
1031 51–57.
- 1032 [68] Y. Jiao, S. Yamada, S. Kishiki, Y. Shimada, Evaluation of plastic energy dissipation capacity  
1033 of steel beams suffering ductile fracture under various loading histories, *Earthq. Eng. Struct.*  
1034 *Dyn.* 40 (2011) 1553–1570. <https://doi.org/10.1002/eqe.1103>.
- 1035 [69] Y.-S. Yu, X.-Y. Liu, Finite element analyses on energy dissipation capacity of upper flange

1036 welded-lower flange bolted beam-column connection with slotted holes, *J. Asian Archit.*  
1037 *Build. Eng.* 19 (2020) 315–326. <https://doi.org/10.1080/13467581.2020.1749639>.

1038 [70] T. Liu, S. Chen, Z. Feng, H. Liu, Effect of Web Openings on Flexural Behaviour of  
1039 Underground Metro Station RC Beams under Static and Cyclic Loading, *Adv. Civ. Eng.* 2020  
1040 (2020) 1210485. <https://doi.org/10.1155/2020/1210485>.

1041 [71] J. Cai, Z. Deng, W. Li, Numerical Study on Seismic Behavior of Demountable Joints  
1042 Consisting of Reinforced Concrete Columns and Steel Beams, *Buildings* 13 (2023) 2558.  
1043 <https://doi.org/10.3390/buildings13102558>.

1044 [72] K.D. Tsavdaridis, T. Papadopoulos, A FE parametric study of RWS beam-to-column bolted  
1045 connections with cellular beams, *J. Constr. Steel Res.* 116 (2016) 92–113.  
1046 <https://doi.org/10.1016/j.jcsr.2015.08.046>.

1047 [73] S. Sarfarazi, R. Shamass, F. Guarracino, I. Mascolo, M. Modano, Exploring the stainless-  
1048 steel beam-to-column connections response: A hybrid explainable machine learning  
1049 framework for characterization, *Front. Struct. Civ. Eng.* 19 (2025) 34–59.  
1050 <https://doi.org/10.1007/s11709-025-1162-y>.

1051 [74] J. Orr, O. Gibbons, W.B. Arnold, A brief guide to calculating embodied carbon, *Struct. Eng.*  
1052 (2020). <https://api.semanticscholar.org/CorpusID:256166957>.

1053

1054